Design of 3D-Printable Conductive Composites for 3D-Printed Battery

By

Jae Sung Park

B.A.Sc., Simon Fraser University, 2014

Thesis Submitted in Partial Fulfillment of the
Requirements for the Degree of
Master of Applied Science

In the
School of Mechatronic Systems Engineering
Faculty of Applied Science

© Jae Sung Park 2016

SIMON FRASER UNIVERSITY

Summer 2016

Approval

Name:	**Jae Sung Park**
Degree:	**Master of Applied Science**
Title:	***Design of 3D-Printable Conductive Composites for 3D-Printed Battery***
Examining Committee:	**Chair:** Mehrdad Moallem Professor

Woo Soo Kim
Senior Supervisor
Assistant Professor

_____

Jiacheng (Jason) Wang
Supervisor
Assistant Professor

_____

Majid Bahrami
Internal Examiner
Professor

_____

Date Defended/Approved: August 9, 2016 _____

Abstract

In this research, a biocompatible nano-composite is designed for the application of 3D printed battery. The nano-composite paste is composed of an electrically conductive silver nanowire (AgNW) filler within a thixotropic carboxymethyl cellulose (CMC) matrix. Experimental demonstration and computational simulations on nano-composites with various filler fractions are performed to find the electrical percolation threshold of the nano-composite. The percolation threshold as 0.7 vol. % of AgNWs is predicted by computer simulations as well as by experiments. Also, maximum electronic conductivity is obtained as 1.19×10^2 S/cm from a nano-composite with 1.9 vol. % of AgNWs. Also, newly designed paste 3D printing apparatus is built by integrating a commercially available delta 3D printer with a paste extruder.

Finally, the 3D printable battery facilitated by the conductive composite is demonstrated. Cathode and anode materials are formulated by addition of cathode and anode active materials to the nano-composite of AgNW and CMC. Rheology study of the cathode and anode paste is carried out and thixotropic (shear-thinning) behavior is observed which is an essential characteristic of the 3D printable paste [1], [2]. Lastly, the performance demonstration on the fabricated 3D printed battery is carried out. The 3D printable conductive paste is expected to contribute in additive manufacturing process for printable electronics.

Keywords: Silver nanowire; CMC; nano-composite; percolation threshold; paste 3D printing; lithium battery

I would like to dedicate my thesis

to Jesus and my beloved family

Acknowledgements

I would like to truly appreciate my senior supervisor, Dr. Woo Soo Kim, for his kind supervision throughout my Master's degree study. He has been always available for my project discussion or even for my personal consultations and tried to think together for sorting things out. I also would like to thank my thesis committee members, Dr. Jason Wang for being my supervisor, Dr. Mehrdad Moallem and Dr. Majid Bahrami for being committee examine Chair and internal examiner who were willing to review my work and joined my defence.

It has been a great moment researching with my beloved lab mates. I would like to thank Abrar, who is an oldest lab mate and was willing to have fun time with me. Taeil, I enjoyed spending time with him who gave friendly and sincere advices. Manpreet, she was always kind to provide help me with a great smile. Yue, we were at a same age and I felt comfortable with him and I enjoyed recreational time in Vancouver. Also, I would like to thank many past co-op students for allowing good memories with them.

I sincerely want to thank God for allowing me a great Master's degree study period in SFU and in this lab. All the work I've done became possible with his grace and I want to devote my work to him. I truly thank my family who were always proud of me and never hesitated providing me any kinds of supports. I also want to remember my dog Sam who passed away on June 15th, 2016. Lastly, I would like to thank Elena for her love and solid trusts toward me. She always stayed by me and provided comfort whenever I'm happy or having sad moments.

Table of Contents

List of Tables

List of Figures

List of Acronyms

AgNW   Silver Nanowire

CAD   Computer-Aided Design

CB   Carbon Black

CNT   Carbon Nanotube

CMC   Sodium Carboxymethyl Cellulose

CV   Constant Voltage

CNT   Carbon Nanotube

DC   Direct Current

DI   De-Ionized

EG   Ethylene Glycol

FDM   Fused Deposition Modeling

IPA   Isopropyl Acohol

Li   Lithium

Li-ion   Lithium Ion

LTO   Lithium Titanate ($Li_4Ti_5O_{12}$)

LFP   Lithium Iron Phosphate ($LiFePO_4$)

PEO   Poly(ethylene oxide)

PLA   Polylactic Acid

PVP   Polyvinylpyrrolidone

RAMBo   RepRap Arduino-compatible Mother Board

RPM   Revolutions per Minute

RVE   Representative Volume Element

SBR   Styrene-Butadiene Rubber

SEM   Scanning Electron Microscopy

SLS   Selective Laser Sintering

TEM   Transmission Electron Microscopy

UV   Ultra-Violet

Chapter 1

Introduction

1.1. Motivation

According to recent reports of 3D printing market trends and forecasts, the 3D printing industry marked total of $5.165 billion with a significant $1 billion growth (25.9 %) in a single year of 2015 [3], and the market is expected to reach $8.6 billion by 2020 [4] suggesting a promising future of 3D printing technology. Although the use of current 3D printers is mainly on a rapid prototyping purposes, the next emerging field for the 3D printing is embedding the different components such as electronics or batteries in a single-build cycle with the use of multi-materials; thermoplastics, dielectric or electricity conducting materials [5]. However, the most affordable and widely-used type of 3D printer [6], the Fused Deposition Modelling (FDM) 3D printer has printing material restricted to the thermoplastics [7], [8] with only a few carbon-based conductive filaments that demonstrate insufficient conductivity to be used for electrical applications [9], [10].

Electrically conductive silver nanowire (AgNW) is broadly researched because of its superior electrical properties and capability of percolated from its network formation from its high aspect ratio (ratio of length to diameter of a cylinder) within a composite matrix [11], [12]. On the other hand, a naturally-abundant sodium carboxymethyl cellulose (CMC) is often used as a thickening or binding agent and possess thixotropic rheology [13]. The merging of conductive AgNW and the thixotropic CMC matrix can result in a 3D printable highly conductive composite paste. A paste 3D printing platform and a AgNW/CMC printable composite can facilitate superior electronic conductivity compared to the existing thermoplastic-based conductive filaments with a minimal modification to the standard FDM 3D printer.

A wide range of material selection provided with the paste 3D printing system [14] and electrical property with the AgNW/CMC conductive paste, the utilization of the conductive composite can be extended to electronics fabrication with a 3D printer. One feasible paste 3D printable electrical component is a battery as it is a structure with layers composed of particles. A demand for lithium battery is rapidly increasing with emerging of portable devices and electric vehicles (EV) [15]. The lithium battery is composed of cathode and anode layers of lithium active particles which can be simply formulated by mixing the active materials with the AgNW/CMC conductive paste.

1.2. Objective

The objectives of this thesis are summarized as below
- Design of 3D printable conductive AgNW/CMC nano-composites
- Evaluation of electrical percolation of developed nano-composites
- Development of paste 3D printer from a delta 3D printer integrated with a 3D paste extruder
- Rheology study and printability optimization of 3D printable conductive pastes
- Performance demonstration 3D printed battery

1.3. Contribution

In this thesis, AgNW-based conductive nano-composite with CMC matrix has been developed and evaluated for the application of 3D printed battery. Simulational and experimental study was performed to find a AgNW-derived percolation threshold of the AgNW/CMC composite. Also, a novel and low-cost paste 3D printing system platform has been established by integrating commercial delta 3D printer and a syringe-type paste extruder. Lastly, fabrication and evaluation of poly(ethylene oxide)-based polymer electrolyte study along with 3D printable battery anode and cathode pastes are achieved. Rheology investigation of the electrode paste, 3D printing process of battery and its performance characterization are demonstrated.

1.4. Thesis Organization

The organization of thesis is as follows. In chapter 1, recent researches on various types of conductive nano-composite are introduced. And advantages of AgNW/CMC over other nano-composites are discussed. Also, review on conventional conductive material 3D printing technology and recent studies on conductive paste 3D printing are discussed. Chapter 2 explains on our paste 3D printing system platform and its integration process of commercial delta 3D printer with a paste extruder. The software control of 3D printer and key parameters for paste extrusion are also introduced. Chapter 3 starts with describing a concept of percolation network and its importance in designing a conductive nano-composite. Percolation behavior of AgNW/CMC conductive nano-composite is studied with computer simulation. And it was compared to experimental studies for investigation of percolation threshold. In Chapter 4, 3D printing of a battery electrode pastes based on the AgNW/CMC composite is demonstrated. Also, studies on polymer electrolyte and its preparation is shown. Preparation of the pastes, rheology study as well as performance study of the 3D printed battery is described here. Conclusion and future work are outlined in Chapter 5.

1.5. Conductive CMC-Matrix AgNW Nano-composite

1.5.1. Conductive Nano-composites

Nano-composite is a solid material that has mixture of two or more phases with at least one phase in nanometer scale (from 1 to 100 nm) [16]. With a size reduction of a material down to nanoscale, the material's thermal [17], mechanical [18] or electrochemical [19] properties can be uniquely defined which were not available in its bulk form. The lower sintering temperature promotes easiness of a manufacturing process for example, a sintering temperature of bulk gold is 1,063 °C while it is only about 130 °C with gold nanoparticles in 2 nm size [17], [20]. Also, addition of conductive nano-fillers in a polymeric matrix can provide an electrical property to the composite. Enormous kinds of conductive nano-composite composed of various fillers have been reported as an alternative for using conductive bulk metals or alloys thanks to the previously stated advantages brought by nanomaterials.

Carbon allotropes such as carbon black (CB) and carbon nanotube (CNT) are being extensively researched conductive nanomaterials for conductive nano-composite applications. Carbon black (CB) is a carbon particle made from an incomplete combustion of petroleum which is spherical with typical size of 20 ~ 60 nm (Figure 1.1) [21], [22].
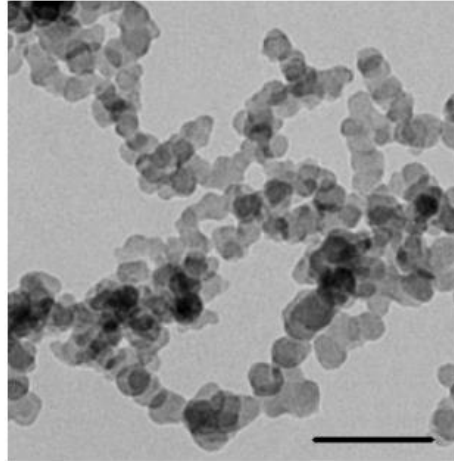
Figure 1.1   TEM image of spherical carbon black particles [23]. Reprinted with permission.

For its cost-effectiveness and fair electricity conducting property, researches have proposed nano-composites with CB conductive filler. P. C. Ma et al. [22] demonstrated a conductive nano-composite with an electrically insulative epoxy (diglycidyl ether of bisphenol A, DGEBA) and conductive CB filler. The composite showed electrical resistivity about 10^6 Ω·cm with 1 wt. % CB content. Considering the fact that the bulk metals possess resistivity in the order of 10^{-6} Ω·cm, the electrical property CB-filled conductive nano-composites can not be sufficient for their use electrical applications. The inferior performance of the CB-based composites can be ascribed to a high electrical resistivity (1 ~ 3 Ω·cm) of CB [22], [24], also its low aspect ratio shape requiring a composite to have high CB content loading (wt. % or vol. %) to form a percolation network. A percolation threshold of a composite with carbon black is typically in a range of 3 to 15 wt. % [25], [26].

Meanwhile, a composite with CNT has electrical conduction advantage with CNT's lower electrical resistance (0.2 Ω·cm) [22] which is about a tenth order of magnitude of CB. Moreover, the CNT has an extremely high aspect ratio (500 ~ 5000) cylindrical shape thus, a composite including CNT can have a benefit of having a lower electrical percolation threshold (less than 1 wt. %) [22], [25].
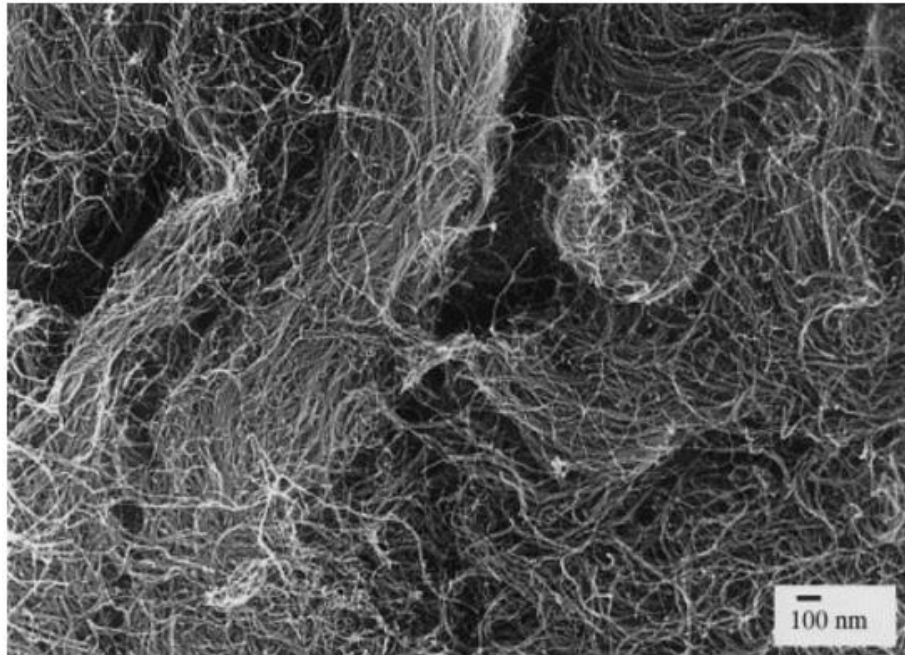
Figure 1.2   (a) SEM image of CNT [27]. Reprinted with permission.

The supressed percolation threshold and higher conductivity of CNT promotes its use in the nano-composite applications. P. C. Ma et al. [22] demonstrated an CNT-filled epoxy-based nano-composite. An electrical resistivity of 10^3 Ω·cm was measure with a low 0.3 vol. % percolation threshold thanks to CNT's high aspect ratio. J. Sandler et al. [27] proposed a CNT-filled nano-composite within an epoxy matrix (bisphenol-A). An electrical resistivity of 10^4 Ω·cm with a significantly low 0.02 wt. % percolation threshold with an aid of optimized CNT distribution in the matrix. However, a high cost of CNT and its still-insufficient electrical resistivity (0.2 Ω·cm) inhibit its uses in composite fabrication [22], [28].

Silver nanowire (AgNW) is actively researched for its uses in nano-composite applications thanks to its promising metallic electrical resistivity of silver (1.6×10^{-6} Ω·cm) and a high aspect ratio (typically, 50 ~ 500) [29]. AgNW has a rod-shape with a pentagonal cross section and unlike CNT, AgNW is straight in nature (Figure 1.3) [29], [30].
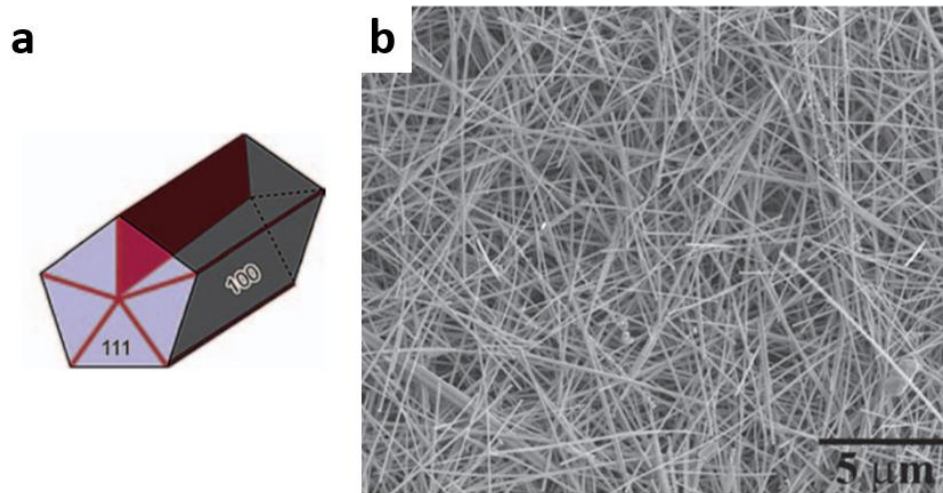
Figure 1.3 **(a) Schematic representation of AgNW [29] and (b) SEM image of AgNWs [30]. Reprinted with permission.**

S. I. White et al. [31] demonstrated an AgNW/polystyrene nano-composite. A percolation threshold was found to be 2.3 vol. % with an aspect ratio of AgNW was 16 and a resistivity of the composite was measured to be around 10^{-3} $\Omega \cdot$cm. W. Xu et al. [11] recently introduced an AgNW nano-composite based on an environmental-friendly carboxymethyl cellulose (CMC)-matrix (Figure 1.4). A percolation threshold in this study was only 0.29 vol. % due to its higher aspect ratio than White's study [31] with an electrical resistivity around 10^{-3} $\Omega \cdot$cm.
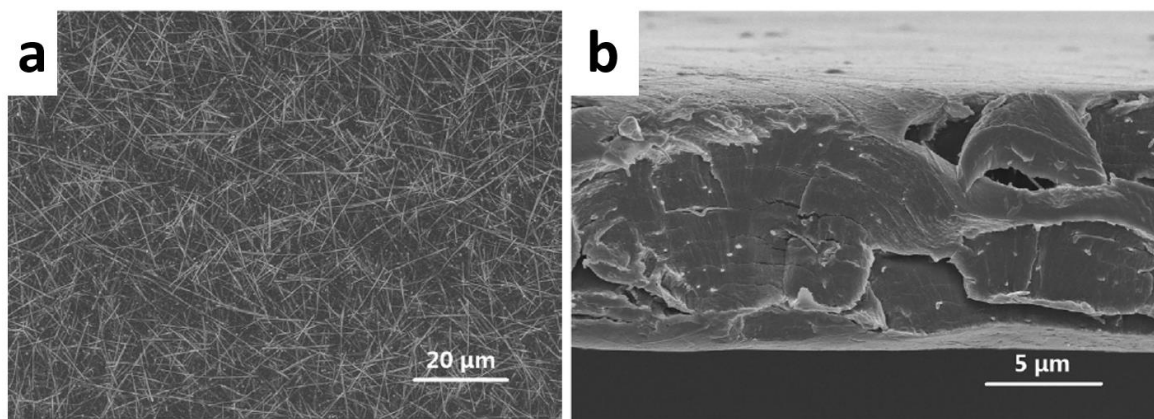
Figure 1.4 SEM images of (a) an AgNW nano-composite and (b) a cross-sectional view of AgNW/CMC composite. Embedded AgNWs are visible in the matrix [11]. Reprinted with permission.

The AgNW-filled composites tend to have a bit higher but fair level of percolation threshold compared to CNT-filled composites due to AgNW's shorter length compared to

CNT. But as AgNW content in the composite exceed beyond the percolation threshold, a superior electronic conductivity can be acquired compared to carbon nano-filler-based nano-composites suggesting AgNW's practical use in conductive nano-composites towards electrical applications.

1.5.2. AgNW and CMC Properties

As mentioned in previous section 1.5.1, AgNW has advantages in composite fabrication for electrical conduction thanks to its high aspect ratio and great conductivity. Another interesting property of the AgNW is its low sintering temperature as compared to a bulk silver. The bulk form of silver has typical 350 °C [32] sintering temperature but AgNW has been demonstrated to have sintering temperature even lower than 200 °C [33]. A general type of AgNW, polyol processed-AgNW is shown on Figure 1.5 (a) [33]. It shows as deposited AgNW with a thin 30 nm-thick shell composed of polyvinylpyrrolidone (PVP) from AgNW synthesis process and an organic residue from a solution (isopropyl alcohol, IPA solvent) based deposition. As can be seen from Figure 1.5 (b), the PVP-coating around each AgNW gets degraded upon a glass transition temperature of PVP (150 °C) and local sintering of individual AgNW junctions can take place at temperature around 200 °C [33].
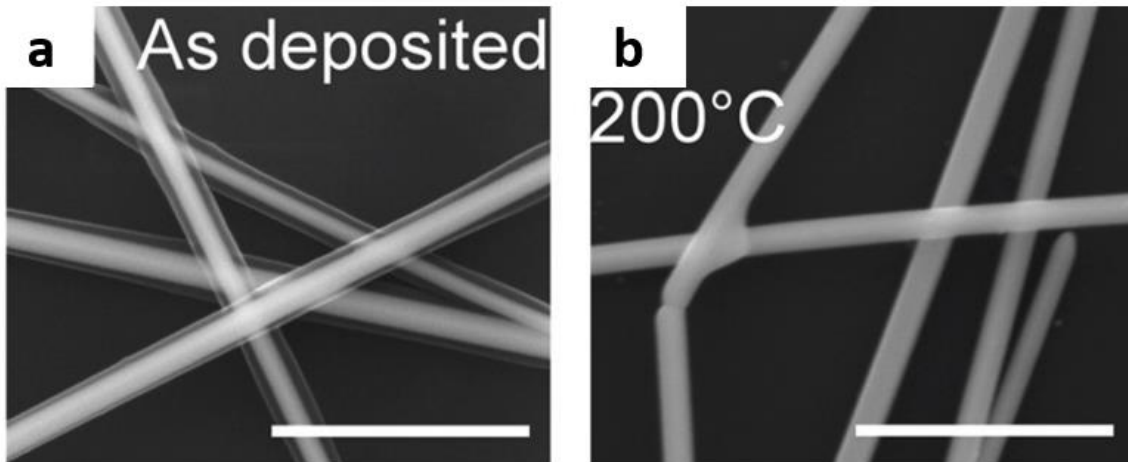
Figure 1.5   SEM images of (a) polyol-processed as deposited AgNWs and (b) AgNWs sintered at 200 °C [33]. Reprinted with permission.

Adjoined AgNWs form a conductive percolation network which is crucial aspect of a conductive composite. Details of percolation network will be discussed in the later section. The low-temperature sintering of AgNW benefits fabrication of a conductive nano-

composite avoiding the burning of a matrix and at the same time easily increasing the electronic conductivity of the nano-composite.

Carboxymethyl Cellulose (CMC) derived from wood cellulose and it is made by a chemical reaction of the wood cellulose and sodium monochloroacetate (Figure 1.6) [34], [35]. CMC is a biocompatible and water-soluble substance and it has been proposed as a viscosity thickening agent for enormous kinds of personal products, cosmetics such as toothpaste and shampoo or even for foods [34], [36]. As can be seen from Figure 1.6, protrusion of carboxymethyl groups (-CH2-COOH) on the side of cellulose backbone, restricts hydroxyl groups to avoid hydrogen bonding with another hydroxyl group of the other cellulose in turn promoting CMC's high water-solubility.
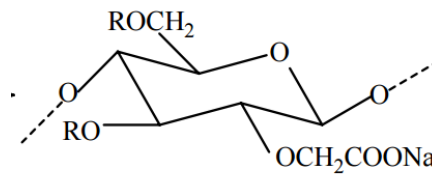
sodium carboxymethyl cellulose

$R = H$ or CH_2 COONa

according to DS_{CMC}

Figure 1.6   **Unit structure of carboxymethyl cellulose (CMC) [35]. Reprinted with permission.**

Another interesting feature of CMC is its thixotropic (shear-thinning) behavior in aqueous solution [37], [38] . For viscous liquid extrusion, the shear-thinning feature plays critical role for its printability through a narrow nozzle [1], [2]. With the thixotropism, a material can flow (lower viscosity) during extrusion with high shear rate and it can stop flowing with the viscosity can return back to high viscosity after extrusion. As shown in Figure 1.7, a CMC solution experiences a large drop in its viscosity with increasing shear rate. For example, CMC solution with 5 wt. % CMC undergoes viscosity change from 90,000 mPa·s (level of toothpaste) at 1 s^{-1} shear rate down to around 15,000 mPa·s (level of mayonnaise) at 10 s^{-1} shear rate [39],
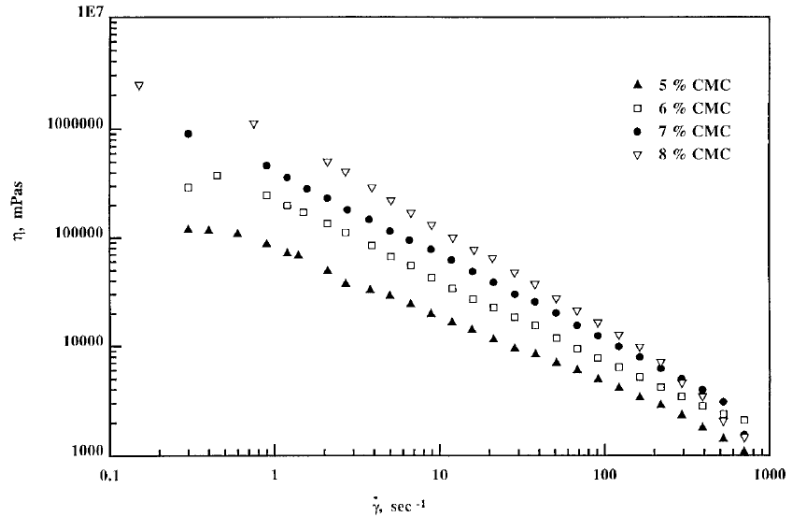
Figure 1.7   Flow curve of representing viscosity with respect to applied shear rate of CMC solution [37]. Reprinted with permission.

CMC has been drawing attentions as replacement material for conventional polymeric binders such as polyvinylidene fluoride (PVdF) which require the use of toxic solvents for their manufacturing [40], [41], [42]. S.S. Jeong et al. [40] and G.T. Kim et al. [42] demonstrated a cathode using CMC as a binding agent for $LiFePO_4$ (LFP) cathode and $Li_4Ti_5O_{12}$ (LTO) anode active particles with greener manufacturing process of using water as a solvent. The fabricated lithium ion batteries showed specific capacities of 123 mAh g^{-1} [40] and 140 mAh g^{-1} [42] and stable charge/discharge cyclic performances up to 50 cycles [40] and 160 cycles [42]. The comparable performance CMC-based lithium batteries to conventional PvDF-based batteries promises CMC's practical use in lithium battery application.
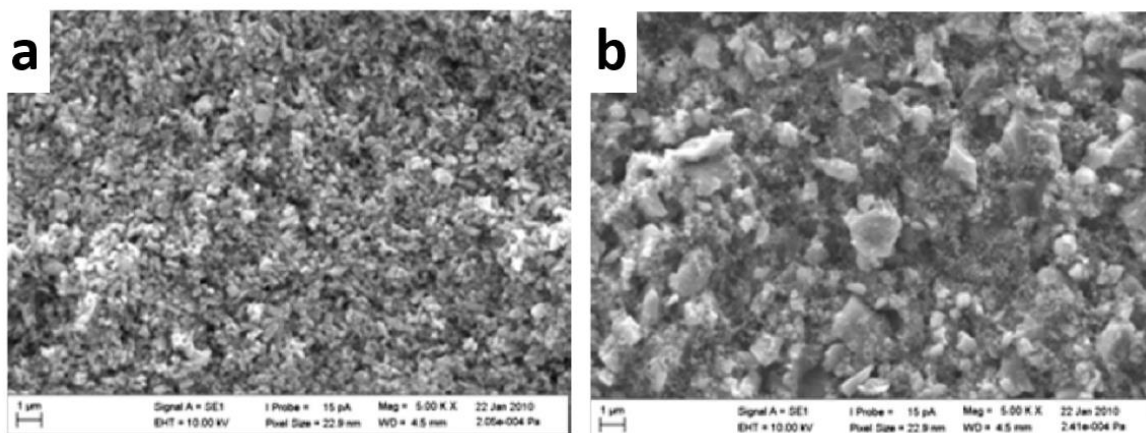
Figure 1.8 **SEM images of (a) a LFP electrode and (b) a LTO electrode with CMC binder [42]. Reprinted with permission.**

In brief, CMC has many attractive features of its biocompatibility, water-processability, successful conductive composite formation with AgNW, shear-thinning feature, binding ability with the battery active materials which brought our attention for fabricating a 3D printable lithium battery.

1.5.3. Preparation of Conductive AgNW Nano-composite Paste

AgNW was synthesized with typical polyol process to create uniform and high aspect ratio AgNWs [29]. Detailed polyol process of AgNW synthesis is discussed in our previous study and AgNW with diameter of 100 ~ 150 nm and length about 20 µm (aspect ratio of 133 ~ 200) was achieved [43]. After the synthesis, AgNW ink was made by dispersing AgNW in de-ionized (DI) water with an ultrasonicator for 1 minutes (Ultrasonic Bath model 2510, Branson ®). Prepared AgNW ink and CMC powder (Mw ~250,000, degree of substitution 0.7, Sigma Aldrich) was vigorously mixed in according volume fractions. For percolation threshold study of the AgNW/CMC nano-composite paste, five composite samples were fabricated with different AgNW content ranging from 0.3 to 1.9 vol. %. As it can be seen from Figure 1.10, the AgNWs are homogeneously dispersed over the CMC matrix proposing a low percolation threshold thus a high electronic conductivity of the AgNW/CMC nano-composite.
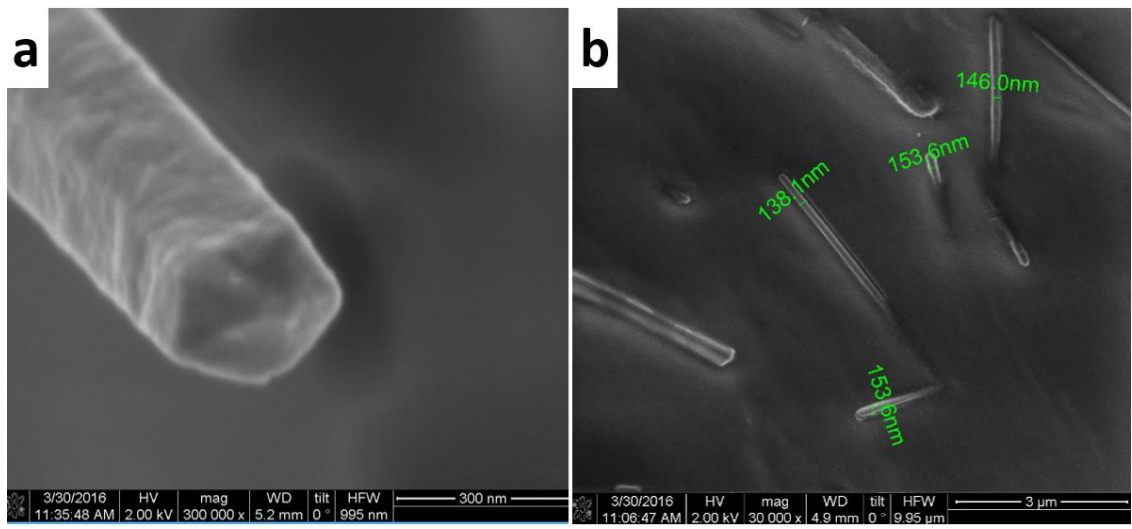
Figure 1.9   SEM images of (a) a synthesized AgNW showing its unique pentagonal cross section and (b) a surface of fabricated AgNW/CMC nano-composite with AgNW diameters labeled.
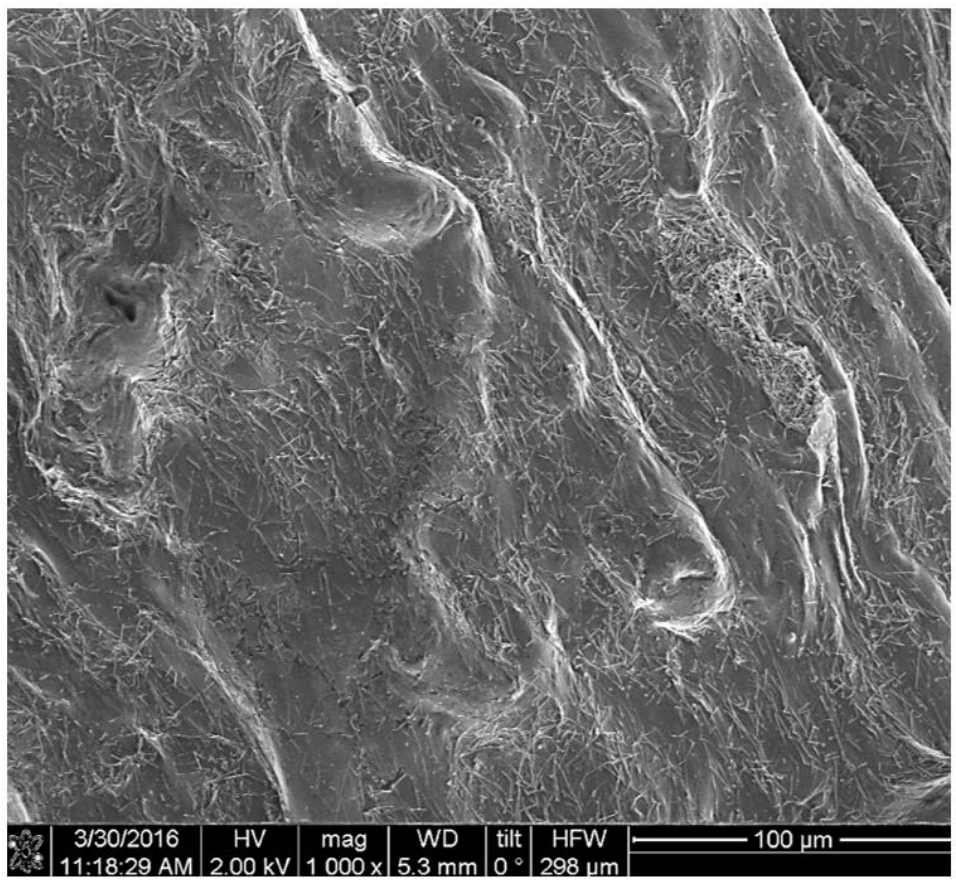
Figure 1.10   SEM image of a surface of fabricated AgNW/CMC nano-composite with 1.9 vol. % AgNW content.

1.6. 3D Additive Manufacturing Process

As opposed to traditional manufacturing processes injection molding, machining, or casting the additive manufacturing has several benefits. Objects with high complexity such as cellular structure are now easier to fabricate without remodeling of molds or several tool changes respectively from casting and machining. Also the additive manufacturing is a bottom-up process of building an object layer-by-layer, a massive material wastes can be avoided unlike the milling or carving processes in the machining [44]. During the past few years, the 3D printing industry experienced a huge compound annual growth rate (CAGR) of 33.8 % in 2014 and 25.9 % in 2015 [3], in turn increasing the need for the 3D printing of functional materials such as printing of electronics like sensors or complex circuits without expensive equipment [45], [46].

One of the most widely used 3D printing technology, Fused Deposition Modelling (FDM) dispenses molten thermoplastic materials through an extrusion nozzle heated above glass transition temperatures of the plastics. The printed filament solidifies immediately after the extrusion. An object is built up with a print head moving with the designed trajectories layer-by-layer [47] (Figure 1.11 (a)).
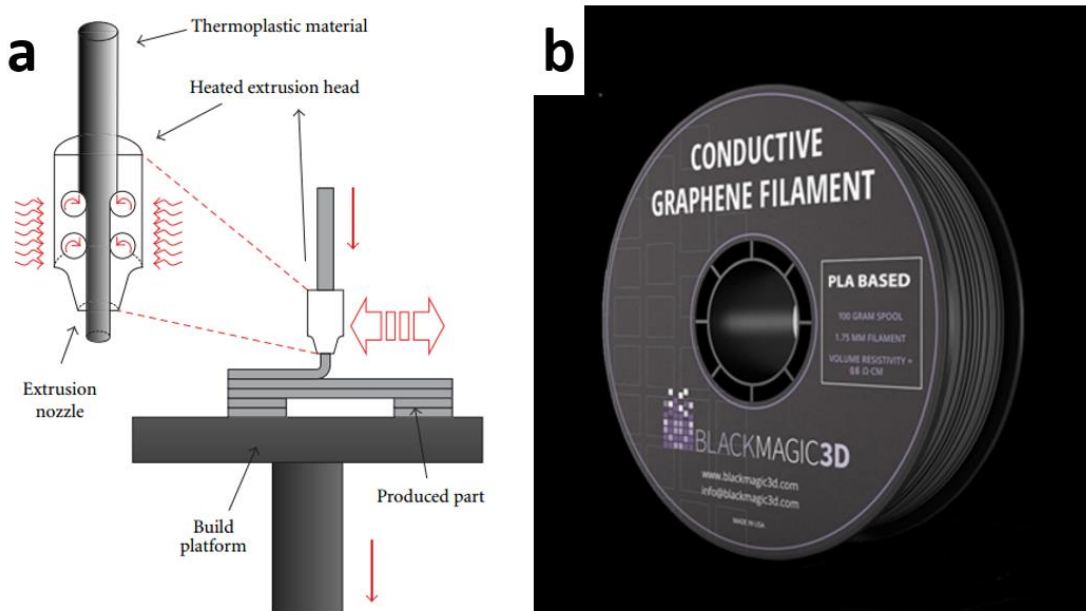
Figure 1.11   **(a) A schematic representation of FDM 3D printing system [47], (b) commercial PLA-based conductive filament for FDM 3D printer [10]. Reprinted with permission.**

Although the conventional Fused Deposition Modelling (FDM) 3D printer is easy, inexpensive, and office-friendly the printing materials of FDM printers solely limit on thermoplastics [7], [8]. There are a few carbon or graphene particle-based conductive thermoplastic filaments developed for FDM 3D printers in the market [9], [10] (Figure 1.11 (b)). However, their inferior conductivity discourages their application in electronics using high current and voltage.

Selective Laser Sintering (SLS) is another 3D printing system that has been proposed for its ability to print various kinds of materials. As shown in Figure 1.12 [47], the SLS system typically uses a carbon dioxide laser that moves through a pre-defined route and scans the surface of a powder bed to fuse thermoplastic powders or to even sinter metal powders that can conduct electricity [48]. After forming a layer by selectively exposing the powders with the laser, the powder bed is lowered by a defined layer height and the new powders are filled from a refilling reservoir located right beside the powder bed. The process is repeated until the printing of a part is completed.
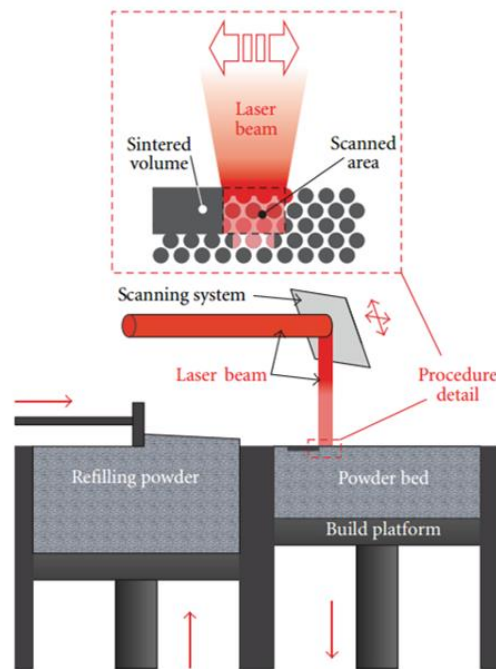
Figure 1.12   A schematic representation of SLS 3D printing system [47]. Reprinted with permission.

Despite the fact that the SLS can eventually print metallic-conductive objects, it requires an expensive and sophisticated printing setup of having a laser and its guiding system, the two lowering powder beds and an inert gas chamber to avoid oxidation of the

metal powders with applied heat [49], [50]. And the system possesses difficulty of material change as it is only available to print a single material until the entire powders are replaced [51].

To overcome the aforementioned limitations of the traditional 3D printing, a composite paste 3D printing has been proposed with its cost-effectiveness and wide range of printing material selection [1], [14], [52]. Depending on materials used for paste composition, printed paste solidifies upon extrusion via paste's solvent evaporation [53], UV-curing [54] or chemical curing of two-mixed agents [52] to form structural layers for stacking. The paste 3D printing system consists of an extrusion syringe for paste material deposition and a syringe pump that controls pressure to the plunge [55].
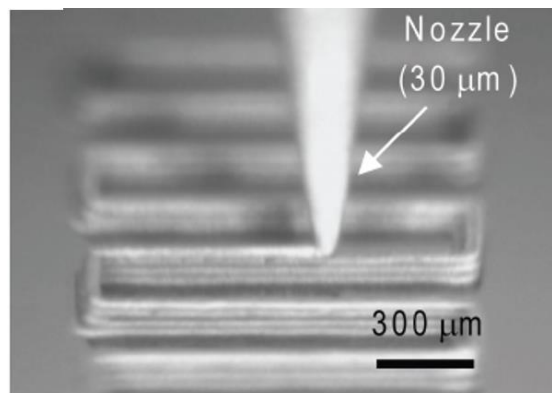
Figure 1.13   View of a paste extrusion system [53]. Reprinted with permission.

At the instance after printing, the nano-composite paste has to maintain its filamentary shape and not laterally spread on the substrate suggesting the highly viscous matrix material and to have shear-thinning (thixotropic) rheology [1], [2], [56], [53].

In this research, to enable 3D printing of the composite paste, the simple and cost-effective paste extrusion system is integrated with the conventional delta FDM 3D printer to create highly conductive 3D object by printing the nano-composite paste. The conductive paste is comprised of the high-aspect ratio AgNW as a conducting filler and the biocompatible CMC matrix. The CMC plays essential role in the composite paste by offering a thixotropic rheology which is the key property of enhancing the 3D printability of the paste. With the 3D printer's free X, Y, Z-axis movement and the nano-composite paste having the strong thixotropism, the integrated paste 3D printing system can create 3D architectures by layer-by-layer stacking the continuous filament.

1.7. Recent Researches on Paste 3D Printed Battery

Direct 3D printing of electronics is a novel idea of manufacturing process which has been suggested with growing 3D printing industry and active development of 3D printable functional materials [46]. Especially, extrusion-based additive manufacturing is claimed to be a most all-around 3D printing technique for its simple mechanism, low-cost and variety material choice [1]. Thanks to the aforementioned advantages of the paste 3D printing technique, recent researches have demonstrated 3D printed batteries with extrusion-based system. K. Sun et al. [53] fabricated a 3D printed interdigitated lithium battery by formulating viscous cathode and anode pastes as can be seen from Figure 1.14. Nano-scaled cathode (lithium iron phosphate, LFP, mean diameter of 180 nm) and anode active (lithium titanate, LTO, mean diameter 50 nm) materials were used to form the paste in order to flow fine extrusion nozzle (30 μm diameter). Concentrated cathode and anode pastes with their solid content loading of 60 and 57 wt. % was used to help avoiding structural distortion or delamination after drying. Glycerol and hydroxypropyl cellulose were used as binding agent and viscosity thickener. As a result, thixotropic anode and cathode pastes were achieved which are 3D stackable. They showed resistivity 2.1×10^5 Ω·cm and 2.3×10^3 Ω·cm respectively after thermal annealing at 600 °C for 2 h.
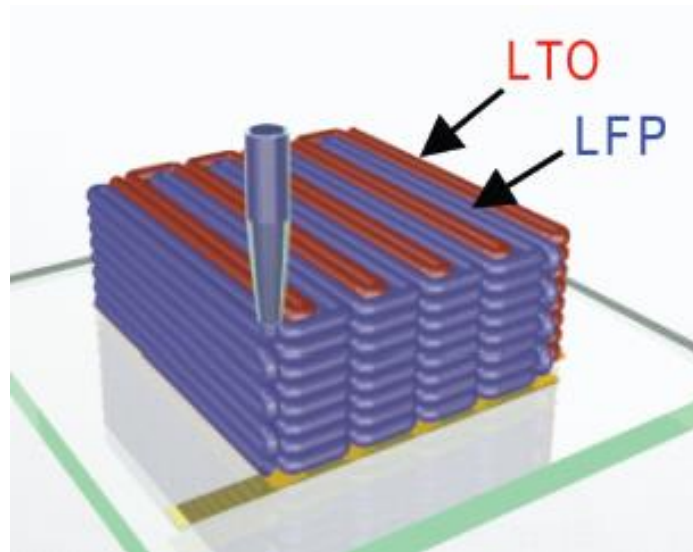
Figure 1.14   (a) Graphical representation of 3D printed battery fabrication and [53]. Reprinted with permission.

A complete battery cell was fabricated by consecutively 3D printing anode and cathode interdigitated layers with 3-axis micro-positioning stage. Battery showed a great

charge/discharge cyclic capability up to 30 cycles and showed high areal capacity of 1.5 mAh cm^{-2} from its 3D geometric structure.

Another interdigitated 3D printed battery was demonstrated by Fu et al. [1]. High viscosity and thixotropic cathode and anode pastes with LFP and LTO active materials were used as well. In this research, however, conductive reduced graphene oxide (rGO) particles were added to the paste to enhance the conductivity of the electrodes. Because of high conductive rGO loading (30 wt. %) in the paste, the resulting cathode and anode electrodes respectively displayed resistivities of 3×10^{-2} Ω·cm and 1.6×10^{-1} Ω·cm which is about 5th order of magnitude less than the pastes from the research conducted by K. Sun et al. [53]. The conductivity increase of the electrodes results in decrease of internal resistance of the battery which promotes increase in battery's electrochemical performance such as battery capacity and charge/discharge capability.

Recent research from Sun et al. [53] and Fu et al. [1] successfully demonstrated 3D printed lithium batteries with comparable performance made by the conductive composite pastes. The shear-thinning property of the composite ink was verified with the viscosity study which enabled layer stacking of the ink to create the 3D printed batteries. The recent research activities suggest the practical use of the highly viscous and shear-thinning pastes to create the printed electronics with the next-generation additive manufacturing process.

Chapter 2

Development of Paste 3D Printer Apparatus

2.1. Paste 3D Printer Configuration

The paste 3D printing apparatus was fabricated by integrating a commercially available delta FDM 3D printer (Orion, SeeMeCNC) and a paste extrusion system (Discov3ry, Structur3d Printing). Also a printing head of the Orion was modified to have two extrusion nozzles; one for thermoplastic extrusion and the other for paste material extrusion.
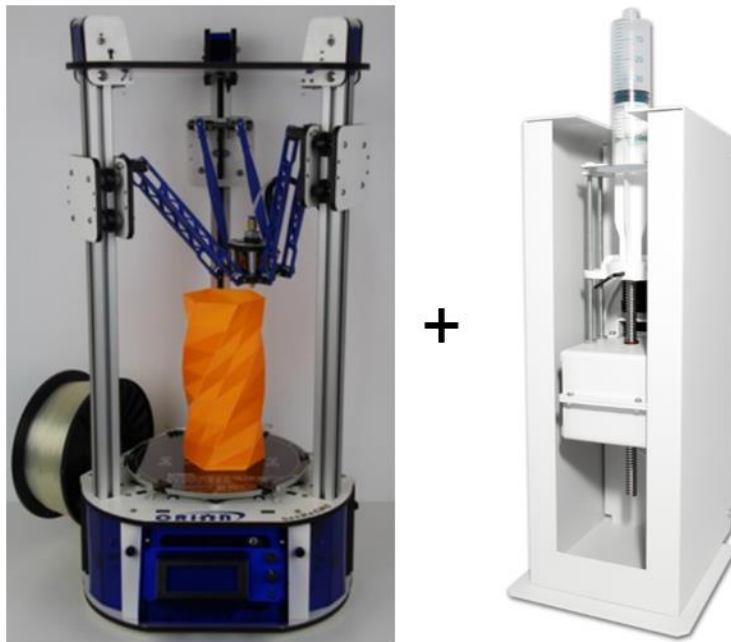
Figure 2.1   **Integration of Orion delta 3D printer (left) [57] and Discov3ry paste extruder with a syringe pump plugged in (right) [58].**

A main electronics board (RAMBo, RepRap Electro) on Orion provides six stepper motor input ports. Among the available ports, four ports are allocated for controlling stepper motors (yellow rectangles in Figure 2.3) each for X, Y, Z-axis and an extruder motor of the Orion. The rest two ports (blue rectangles in Figure 2.3) are left empty for additional machines. The integration of paste extruder starts with electrically connecting

wires of its stepper motor to the available E1 Motor port on the RAMBo. After the connection setup, the Orion's firmware had to be updated to have control on the newly added Discov3ry's extruder on E1 Motor port. The firmware configuration was done by editing Configuration.h and pins.h header files with a compiler software (Arduino IDE) [59].
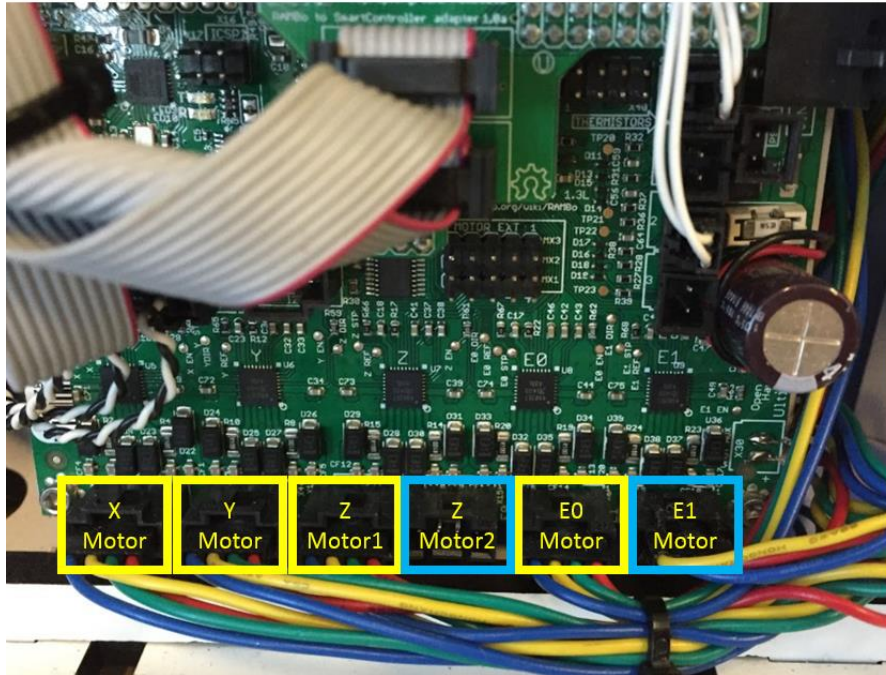
Figure 2.2   Image of six stepper motor input ports available on RAMBo board.

The original Discov3ry paste extruder uses a syringe pump to directly extrude paste materials through an extrusion nozzle which leads to an undesired material wastage (up to 3 mL) on the long tubing between the pumping and the extrusion syringe (Figure 2.4 (a)). To avoid the material wastage, a hydraulic pumping mechanism was adopted in our paste extrusion system (Figure 2.4 (b)). The hydraulic pumping has two syringes; a 60-mL pumping syringe receives a primary pressure from the Discov3ry motor at one end while an extrusion syringe extrudes a material through a nozzle at the other end. These two syringes are connected with the tubing which is filled with water (Figure 2.4 (c)). The extrusion syringe was simply made by placing two 5-mL syringe back-to-back to form a barrel and a plunger was inserted in the barrel for pressure transmission (Figure 2.4 (d)).
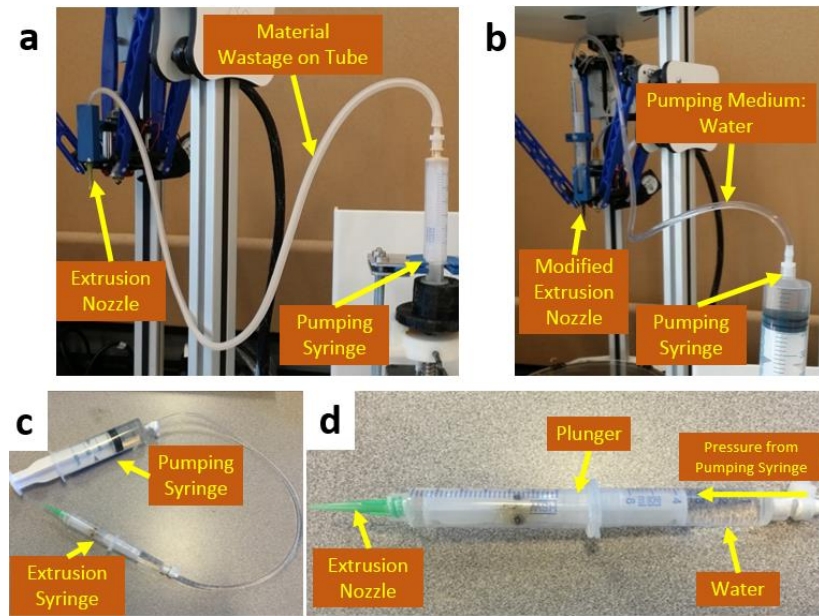
Figure 2.3 **Explanation of (a) original Discov3ry extrusion system, (b) modified hydraulic pumping extrusion system, (c) hydraulic syringe pump and extrusion syringe, and (d) detailed view of the modified extrusion syringe.**

Orion 3D printer has a single thermoplastic extrusion nozzle. Thus, an additional nozzle for paste extrusion had to be added to the printing head. A plastic holder for 5-mL extrusion syringe was designed so that it can be simply mounted at one side of the printing head without major structural modification of the printing head. The holder was designed with a 3D CAD software (Solidworks) and 3D printed with polylactic acid (PLA) filament as shown in Figure 2.5. The paste 3D printing apparatus was completed after mounting the 3D printed syringe holder and the paste extrusion syringes in place (Figure 2.6).
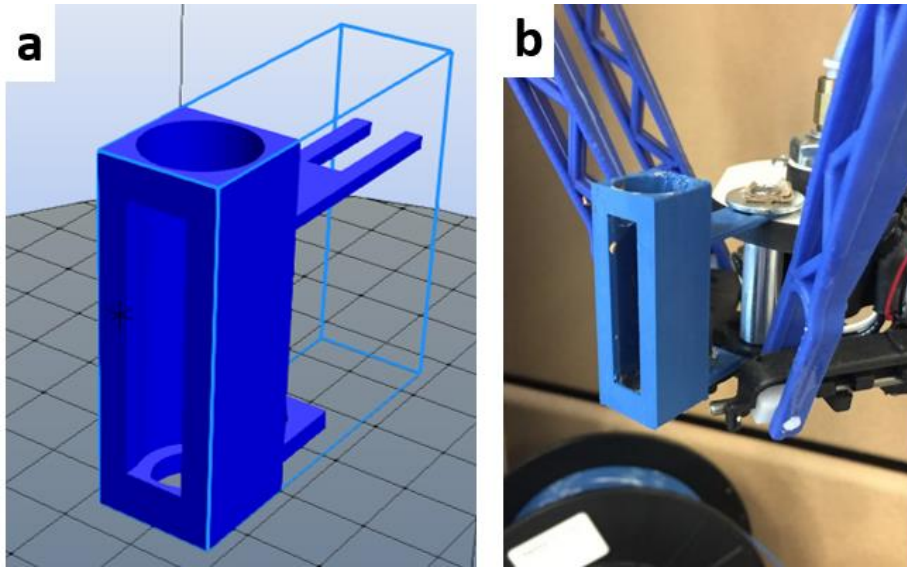
Figure 2.4 **Images of (a) CAD design of 3D paste holder and (b) actual 3D printed syringe holder mounted at the print head.**
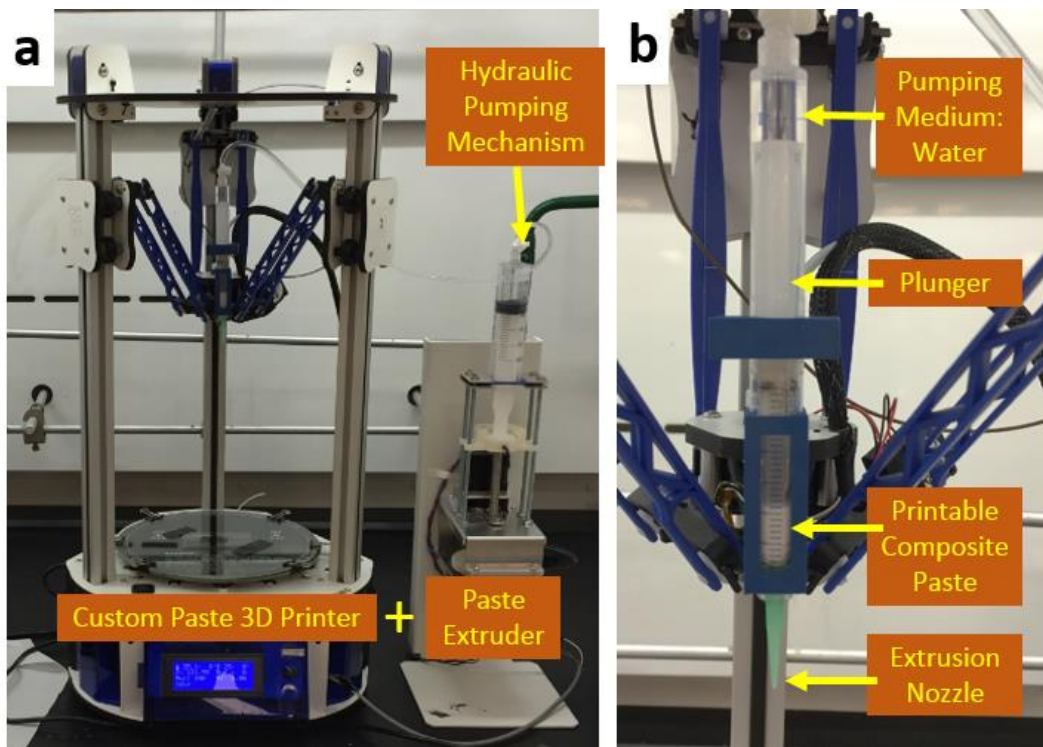
Figure 2.5 **(a) Complete paste 3D printing apparatus and (b) close-up view of extrusion syringe mounted at the print head.**

2.2. Control of Paste 3D Printing Apparatus

The control of the paste 3D printer was done with a host software (Repetier Host) which is one of the widely used open-source software to control 3D printers in the market (Figure 2.7). The role of the host software is to control the arms and peripherals (heated bed temperature, fans and etcs.) of the 3D printer with a generated machine code (g-code) by the slicer software which is integrated in the host software. The Repetier Host comes with two integrated slicer softwares (Cura and Slic3r) [60]. Users can import their CAD design in .STL (stereolithography) format to the slicer software in which the design can be sliced layer-by-layer and can create a g-code for printer head's printing/traveling trajectories as well as heated printing nozzle temperature, bed temperature, fan speed settings, and various other peripheral settings. In addition to automatically executing the g-code, Repetier provides a manual control panel for calibration purpose and printing parameters such as material extrusion and printing head movement speed so that the user can troubleshoot the print during the printing process. A back pressure build-up is one drawback of the hydraulic pumping mechanism [61]. Especially, in order to extrude a high-viscous paste with the hydraulic pump, a certain amount of manual extrusion has to be applied prior to actual printing to overcome the significant back pressure built inside the hydraulic extrusion syringe.
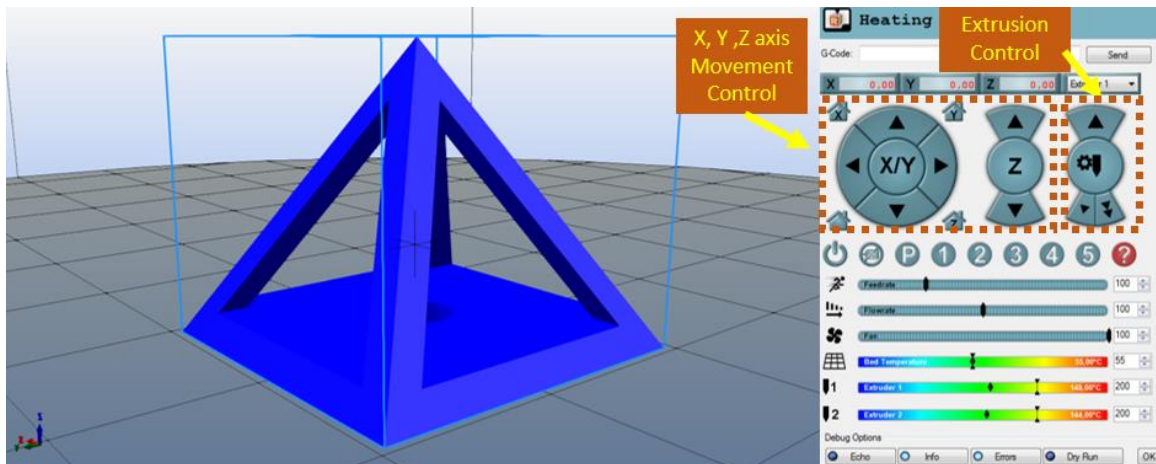
Figure 2.6   View of a main window of Repetier Host. An example pyramid structure imported on Repetier Host (left) and manual control panel (right).

The host software generates 3D preview of the design after slicing so that the user can see the design before the actual printing and check potential size, resolution, and

quality of the structures. Among the numerous number of printing setting parameters, the layer height plays a critical role for adhesion of extruded paste on the bed or between the layers. Layer height is basically a layer thickness for each sliced layer of a structure (Figure 2.8 (a)). The rule-of-thumb layer height we have found in this research was the 80 %-size of the diameter of extrusion nozzle (Figure 2.8 (b)). For example, if 0.84 mm-sized nozzle was used then each layer height would be about 0.67 mm (80 %-size of 0.84 mm). If the layer height is too large the extruded paste cannot adhere to the bed or to the previously printed layers due to the strong cohesive force of the paste itself from its high viscosity.
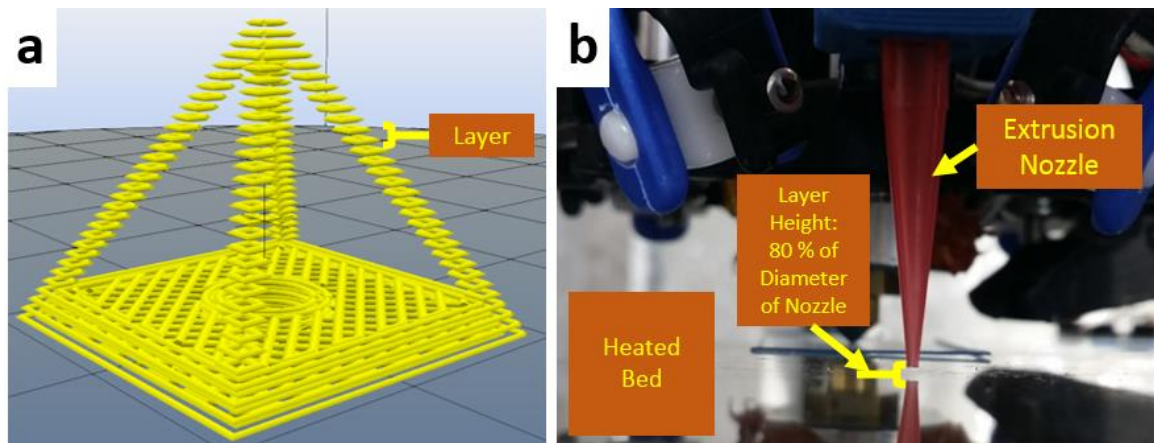
Figure 2.7 **Images of (a) a preview of an example sliced pyramid structure demonstrating layers and (b) a desirable layer height (80 %-size of the diameter of nozzle) for the optimal inter-layer adhesion.**

Chapter 3

Design and Evaluation of AgNW/CMC Nano-composite Paste

3.1. Objective and Plan for Discovering Electrical Percolation Threshold

In this section, a concept of electrical percolation is explained and a discovery of percolation threshold is demonstrated by a computer simulational and an experimental approaches. A composite polymer matrix with a conductive filler inclusion, the conductive particles can form conductive paths when they are in contact or even at adjacent where electrons can jump in between and show tunneling effect [62] (Figure 3.1).
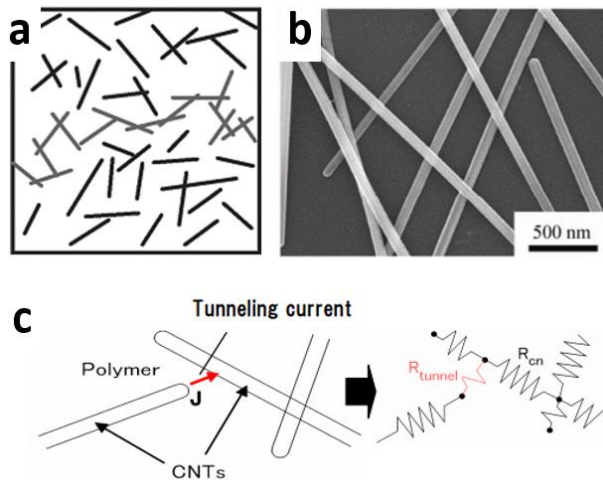
Figure 3.1 **(a) Schematic demonstration of a percolation network (grey colour) in a composite matrix [63], (b) a SEM image of AgNW network [64] and (c) a schematic of tunnelling effect in between adjacent conductive fillers [62]. Reprinted with permission.**

Moreover, the electrical percolation threshold is the minimum filler content (generally, vol. %) in a matrix composite where percolation network is dominant and property of the composite transits from insulative to conductive with increasing filler content loading (Figure 3.2) [65]. With this interesting phase transition, enormous studies about the composite development have been conducted with different kinds of conductive fillers in a rod-shape such as carbon nanotube (CNT) [62], silver nanowire (AgNW) [66]

as well as in a low-aspect ratio form such as silver nanoparticle (AgNP) [66], graphene platelets [63].
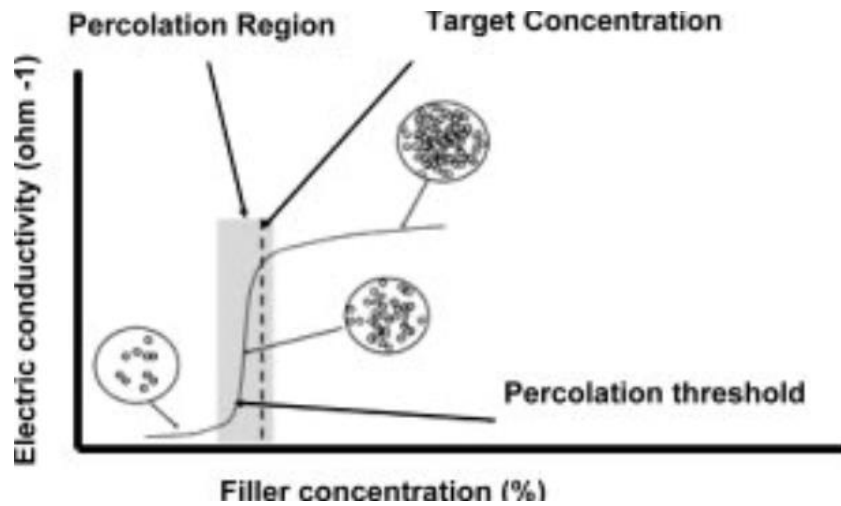
Figure 3.2   **Plot of conductivity with respect to filler volume fraction. Conductivity of a composite sharply increases beyond the percolation threshold marked in a circle [65]. Reprinted with permission.**

In order to form a percolation network, it is not necessary for fillers to have a rod-shape. Percolation can take place regardless of the shape and it can occur with low aspect ratio fillers if a sufficient content loading is satisfied (Figure 3.3) [67].
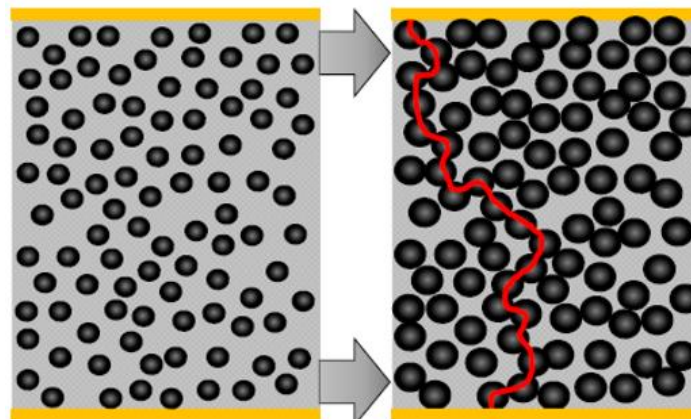
Figure 3.3   **Schematic demonstrating how percolation network (red trace) can occur with low aspect ratio fillers with increasing volume content [67]. Reprinted with permission.**

The rod-shaped fillers (high aspect ratio), however, can form percolation networks with much lower volume fraction compared to the composites including spherical particles or platelets. A. Lonjon et al. researched a relationship between aspect ratio to conductivity of Ag-filled composites. A composite made of silver nanowires have significantly less percolation threshold (0.6 vol. %) while it is found to be 12 vol. % for a composite with silver nanoparticles suggesting the high aspect ratio AgNW as a great conductive filler candidate for a composite formulation (Figure 3.4) [66].
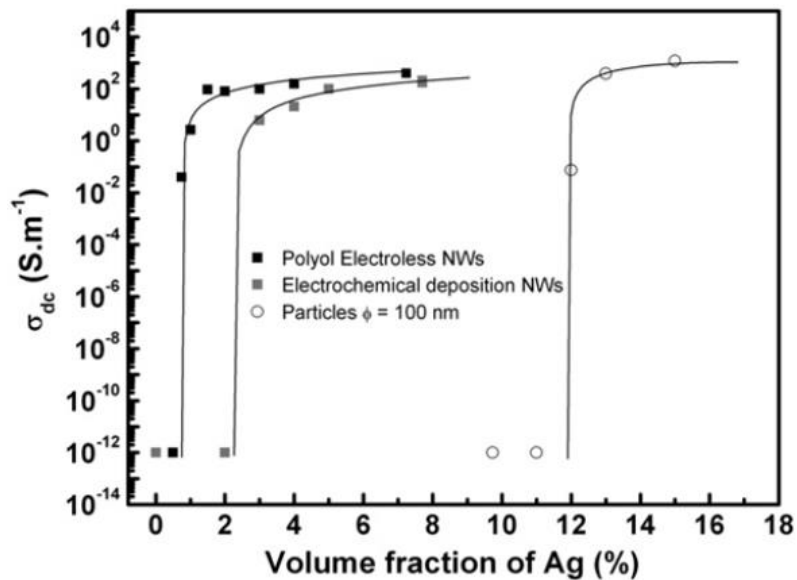
Figure 3.4   **Plot of conductivity of composites with respect to filler content. Dark square-dots represents AgNW with aspect ratio up to 300, grey square-dots for AgNW with aspect ratio of 250, and circle-dots for AgNP with aspect ratio close to 0. Each specimen shows 0.6, 2.2, 12 vol. % respectively [66]. Reprinted with permission.**

Although electrical percolation studies of enormous kinds of fillers and matrices have been reported, to best of our knowledge, no report has demonstrated percolation studies of high aspect ratio (around 200) AgNW within CMC matrix. Thus, we aim to establish a percolation threshold of the composite with high aspect ratio AgNW by experiments and with computational simulations. For the experiments on AgNW/CMC nano-composites, the composite samples are prepared with various filler fractions (from 0.3 vol% to 1.9 vol%) and their electrical conductivities are measured to find a percolation threshold. Also, several CAD nano-composite models are designed with various filler fractions to simulate electronic conductivity of the nano-composite.

3.2. Computational Simulation on Percolation Threshold

3.2.1. Electrical Conduction Simulation Set Up and Process

Computational simulation for electronic conductivity started with designing a AgNW/CMC composite with a composite modeling software (Digimat-FE, e-Xstream engineering). Digimat allows a user to automatically create 3D Representative Volume Element (RVE) composed of a matrix phase filled with various filler material phases. RVE is a volume element that is used for simulation or measurement on behalf of a whole material [68]. In Digimat, various parameters can be set for filler material's properties such as aspect ratio, volume fraction, orientation, and shape (cylinder, sphere, platelet and etc.). In this composite modeling, RVE size was set to $40{\times}40{\times}40$ µm^3 and randomly-oriented cylindrical filler was set to aspect ratio of 200 imitating our AgNW geometry. Figure 3.5 shows 1.9 vol.% AgNW/CMC composite model generated by Digimat.
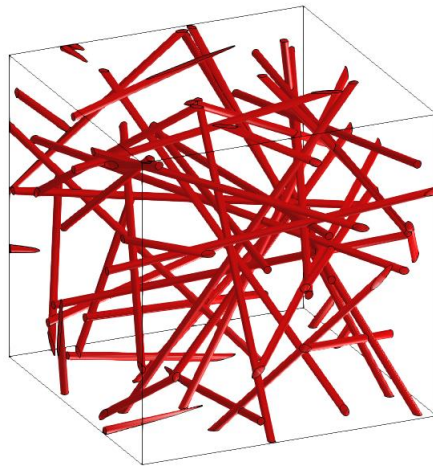
Figure 3.5   A Digimat-generated RVE of AgNW/CMC composite with 1.9 vol. % AgNW content.

After the composite model generation by Digimat, matrix and filler separate geometric files were exported in .step (.stp) format for and a CAD software Autodesk Inventor (Autodesk Inc.) was used to import the geometry .step files to generate CAD model of our AgNW/CMC composite. For electrical conduction simulation, two thin copper electrodes were additionally attached at two ends of the composite model (Figure 3.6).
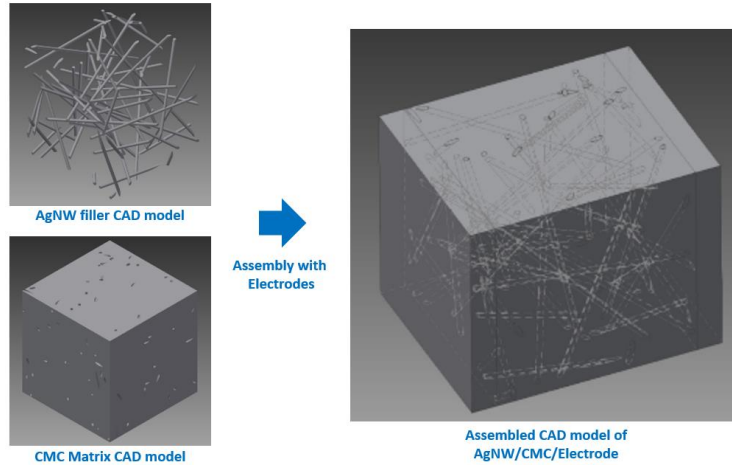
Figure 3.6 Procedure of generating AgNW/CMC composite CAD model for electrical conduction simulation.

Electrical conduction characterization was carried out by a simulation software Ansys Workbench (ANSYS, Inc.). In Ansys Workbench, electrical resistivities of each part of the model were set to 1.58×10^{-6} $\Omega \cdot cm$ for AgNW [29], 1.015×10^{11} $\Omega \cdot cm$ for CMC [69], and 1.68×10^{-6} $\Omega \cdot cm$ for copper [70] respectively. As illustrated on Figure 3.7, for electrical conduction simulation, a voltage drop across the composite was measured while 0 volt was set to 2nd copper plate and current of 1 µA was applied to the 1st copper plate.
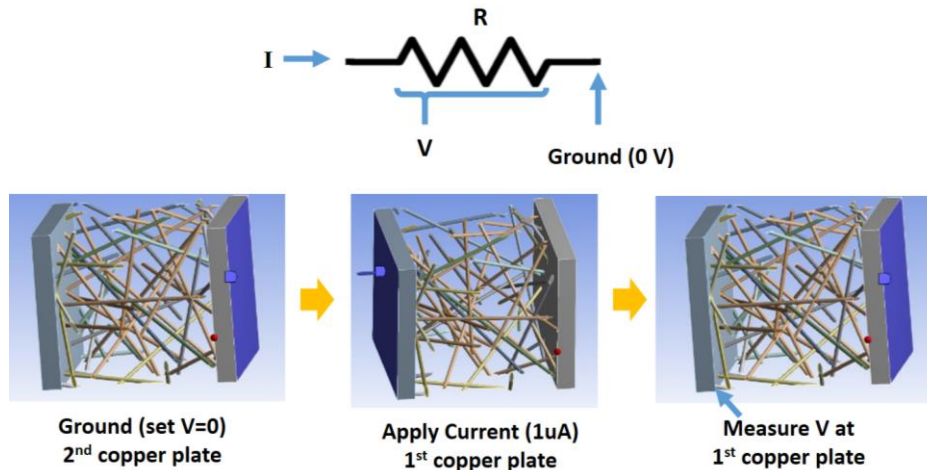
Figure 3.7 Illustration of current source and ground setup for electrical conduction simulation of the AgNW/CMC composite (CMC visual hidden for better understanding).

After running the simulation, a voltage value was measured at the 1ˢᵗ copper plate and composite's resistance (R) was computed with a simple Ohm's law (equation (1)) and resistivity (ρ) was then calculated for the composite (equation (2)).

$$R = \frac{V}{I} \qquad (1)$$

$$\rho = R \cdot \frac{Cross\ Sectional\ Area\ of\ RVE}{Length\ of\ RVE} \qquad (2)$$

where V is the voltage at 1st copper plate, I is applied current.

3.2.2. Simulation Result of Percolation Threshold

By looking at current density distribution over the test model, we could see that the current was flowing through the percolation of AgNW network as can be seen from Figure 3.8. Moreover, higher number of percolations and electrical couplings between 1ˢᵗ and 2ⁿᵈ plates were observed with increasing AgNW concentration.
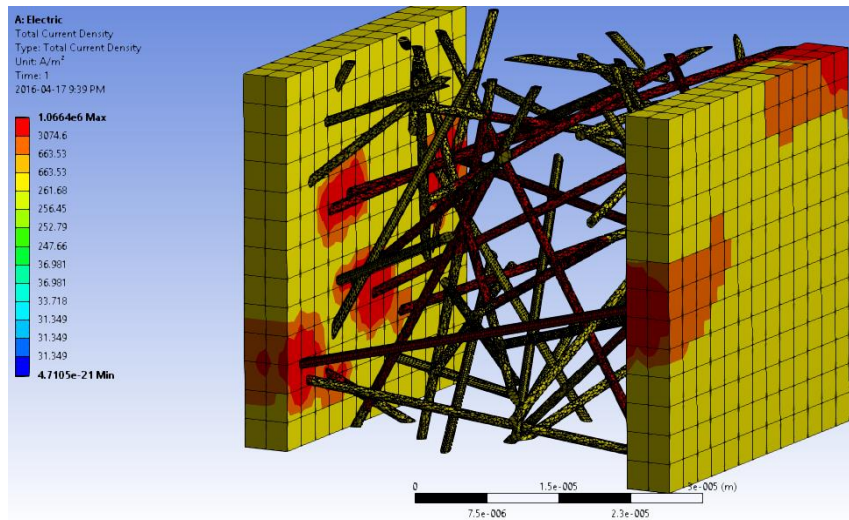
Figure 3.8 **Current density distribution over test sample indicating where current is flowing and how percolation network is formed in composite.**

For electrical percolation threshold study, simulation was performed on composite models with various AgNW contents as 0.3, 0.5, 0.7, 0.8, 0.9, 1.1, 1.5 and 1.9 vol. % (Figure 3.9).

| 0.3 vol. % | 0.5 vol. % | 0.7 vol. % | 0.8 vol. % |
| 0.9 vol. % | 1.1 vol. % | 1.5 vol. % | 1.9 vol. % |
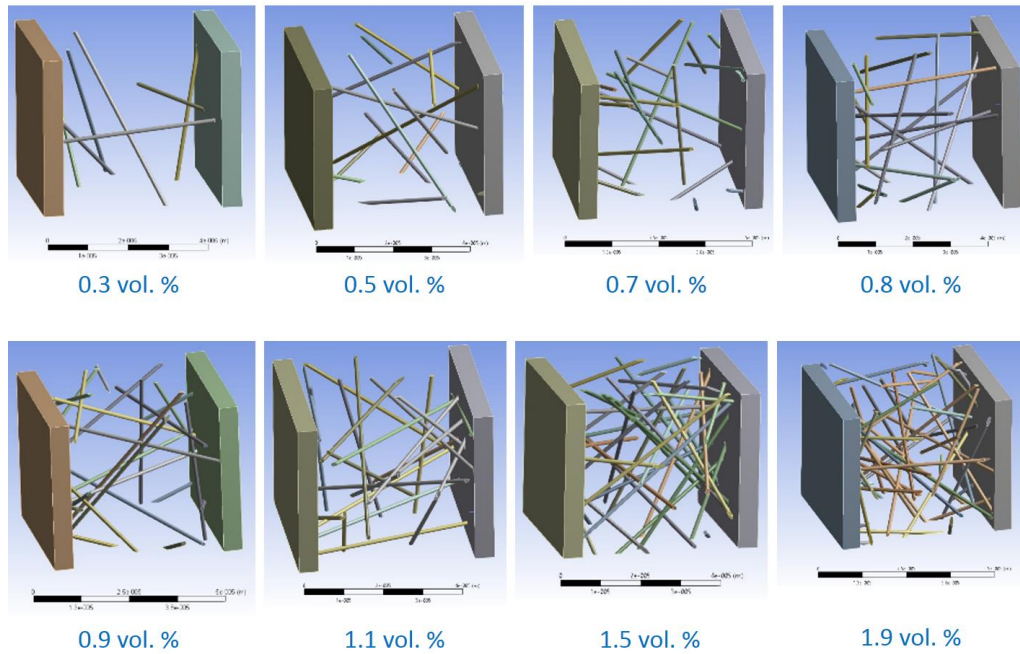
Figure 3.9   AgNW/CMC composites with different vol. % of AgNW for Ansys electrical conduction simulation.

And for each AgNW vol. % composite model, two samples were used and their average was taken to discover simulated resistivity of the composite. A plot of electrical resistivity simulation result is shown in Figure 3.10.
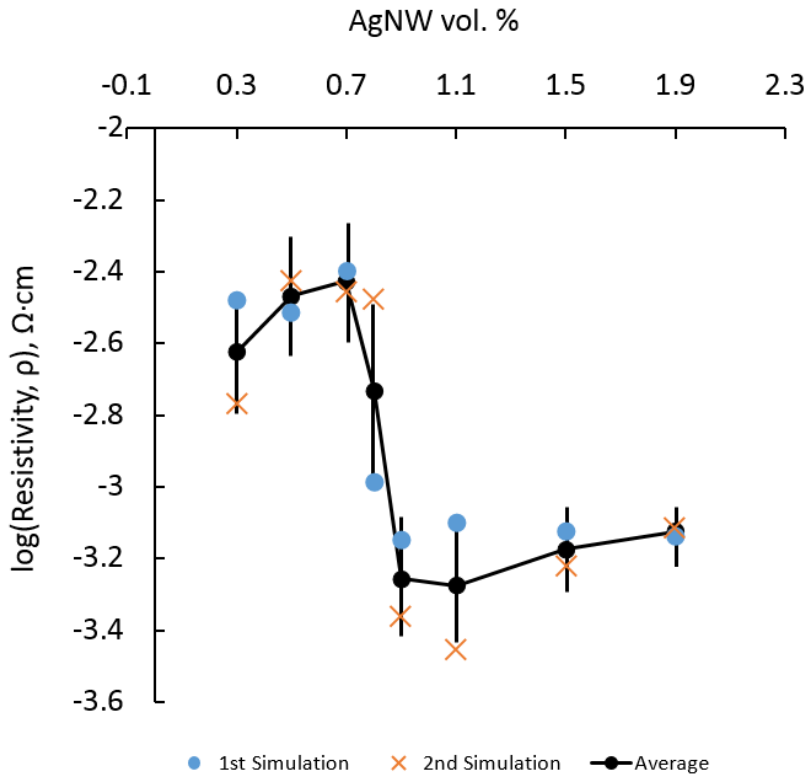
Figure 3.10   Plot of log-scaled resistivity values of composite with respect to different AgNW vol. %.

The simulated result shows a clear trend of decreasing resistivity with increasing AgNW content in the composite. The average resistivity at 0.7 vol. % was 3.75×10^{-3} $\Omega \cdot$cm and with a slight AgNW content increase the value dropped to 5.73×10^{-4} $\Omega \cdot$cm at 0.9 vol.%. The significant drop of resistivity indicates that the AgNW/CMC composite possesses a percolation threshold of 0.7 vol. % and the comparably low percolation threshold will benefit formulation of conductive composite with high aspect ratio AgNW.

3.3. Experiment on Percolation Threshold

3.3.1. Experimental Result of Percolation Threshold

To find out the percolation threshold of the AgNW/CMC nano-composite paste was prepared with five different AgNW filler contents ranging from 0.3 vol% to 1.9 vol%. The AgNW and CMC volume fractions of each sample were calculated using density and

weight fraction values of AgNW and CMC particles as shown in each equation (3) and equation (4).

$$V_{f,\ AgNW} = \frac{\frac{W_{f,AgNW}}{\rho_{AgNW}}}{\frac{W_{f,AgNW}}{\rho_{AgNW}} + \frac{W_{f,CMC}}{\rho_{CMC}}} \qquad (3)$$

$$V_{f,\ CMC} = \frac{\frac{W_{f,CMC}}{\rho_{CMC}}}{\frac{W_{f,AgNW}}{\rho_{AgNW}} + \frac{W_{f,CMC}}{\rho_{CMC}}} \qquad (4)$$

where $V_{f,\ AgNW}$, $V_{f,\ CMC}$, $W_{f,AgNW}$, $W_{f,CMC}$, ρ_{AgNW}, and ρ_{CMC} are AgNW volume fraction, CMC volume fraction, AgNW weight fraction, CMC weight fraction, AgNW density (10.6 g/cm^3) [31], and CMC density (1.6 g/cm^3) [71] respectively. A complete list of samples and their content loading is summarized in Table 3.1.

Table 3.1   Prepared AgNW/CMC composite with five different volume content

	vol. %, CMC	vol. %, AgNW	wt. %, Solid Particles
Sample 1	99.7	0.3	25
Sample 2	99.3	0.7	25
Sample 3	98.9	1.1	25
Sample 4	98.5	1.5	25
Sample 5	98.1	1.9	25

Water was used as a solvent for AgNW and CMC in all prepared paste samples and a solid particle weight fraction among the total mass of the paste (($Mass\ of\ AgNW + Mass\ of\ CMC$) / Mass of Paste) was set to 0.25 in order to create high viscosity for the best 3D printability and layer stacking ability.

From each AgNW vol. % sample, five cylindrical-shaped specimens are prepared by extruding the paste with a syringe. A SEM (Nova NanoSEM, FEI) image of an cylindrical-shaped extruded AgNW/CMC composite paste and a zoomed-in SEM image of a surface of the paste are shown in Figure 3.11 (a) and (b) respectively. It can be observed that the high aspect ratio-AgNWs are embedded in the CMC matrix and are

forming contacts for percolation network. Figure 3.11 (c) and (d) each shows surface a SEM view of composite with 0.3 vol. % and 1.9 vol. % AgNW content loadings.
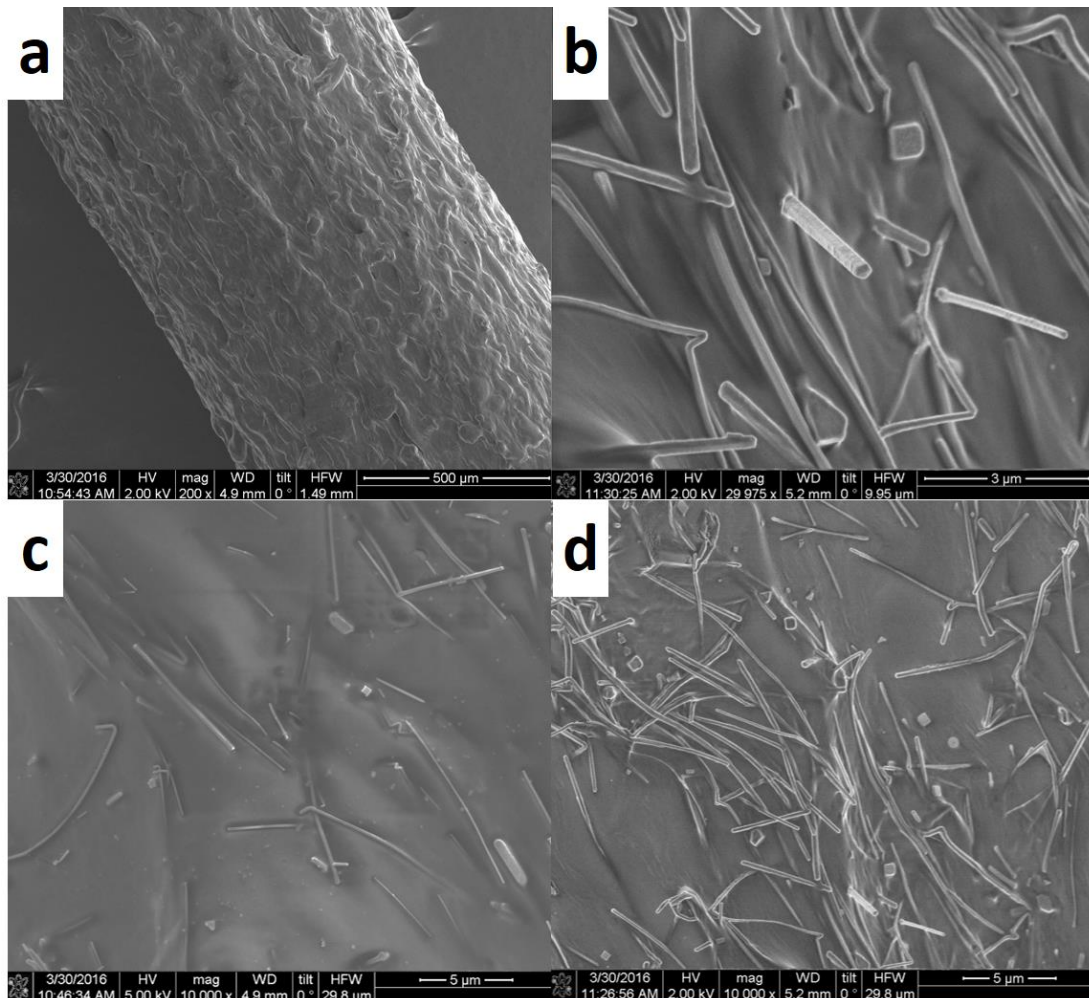
Figure 3.11   **SEM images of (a) extruded cylindrical-shaped AgNW/CMC composite paste, (b) AgNWs embedded in CMC matrix, (c) a composite with 0.3 vol. % AgNW, and (d) a composite with 1.9 col. % AgNW.**

The composite with 1.9 vol. % AgNW clearly has lot more AgNWs being entangled together and forming enormous percolation contacts compared to the composite with 0.3 vol. % AgNW.

Upon complete dry of the extruded pastes, its length and diameters were measured by a digital micrometer (EZ Cal Caliper, iGaging) as shown in Figure 3.12.
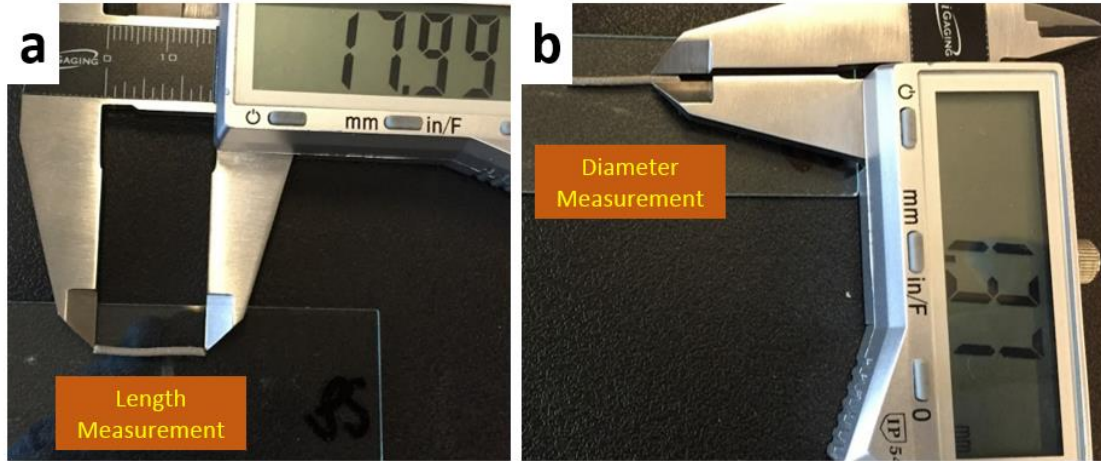
Figure 3.12   Composite paste dimension measurements of (a) length and (b) diameter for resistivity computation.

To compute resistivities of the samples, a sourcemeter (Keithley 2400 SourceMeter) was used with two-wire DC resistance measurement method and equation (5) was used.

$$\rho^* = R \cdot \frac{A}{l} \qquad (5)$$

where ρ^* is resistivity, R is resistance, A is cross sectional area of the sample, and l is the length of the sample. As can be seen from Figure 3.13, mean resistivity values were found (black solid line) from the resistivities of the five specimens (colored dots) for each 0.3, 0.7, 1.1, 1.5 and 1.9 AgNW vol. % samples. The percolation threshold was found to be 0.7 vol. % and a significant drop of resistivity reduction about 9th order of magnitude (from 4.33×10^7 Ω·cm @ 0.3 vol. % to 8.18×10^{-3} Ω·cm @ 1.9 vol. %) was observed with increasing AgNW vol. %. Researches have been reported that the resistivity of the AgNW percolation network can be reduced with a thermal [eo at the temperature above 150 °C which can weld the junction of AgNWs in contact [33], [72], [73] . Thus, the fabricated paste sample were thermally annealed in a hot oven at 160 °C for 50 minutes. The complete resistivity data is listed in Table 3.2.
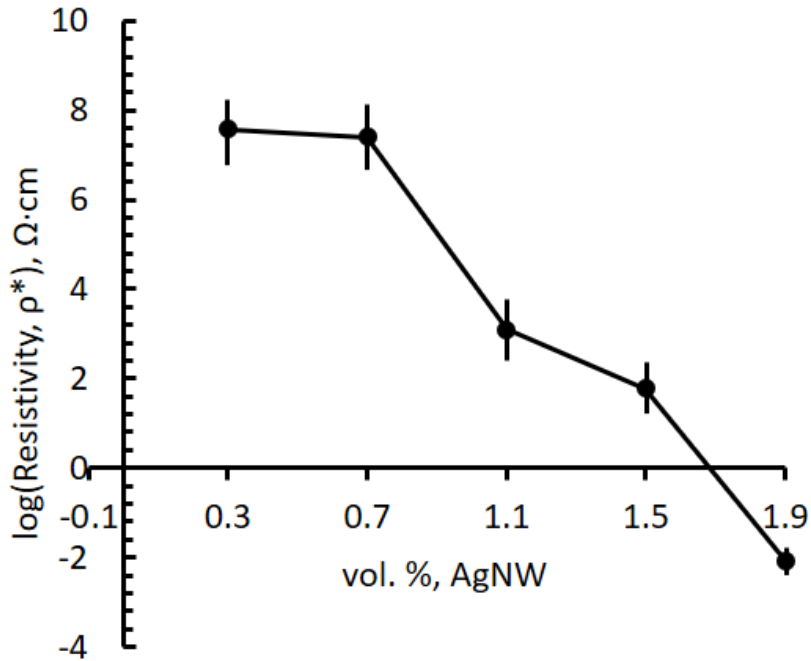
Figure 3.13 **Plot of resistivity with respect to different vol. % of AgNW demonstrating the percolation threshold of 0.7 vol. % and a dramatic resistivity drop with increasing AgNW vol. %.**

Table 3.2 **Resistivity of prepared AgNW/CMC composites**

	AgNW (vol. %)	Resistivity ($\Omega \cdot cm$)
Sample 1	0.3	3.74E+07
Sample 2	0.7	2.57E+07
Sample 3	1.1	1.25E+03
Sample 4	1.5	5.92E+01
Sample 5	1.9	8.38E-03

The experimental resistivity data of the AgNW/CMC composite demonstrated a good agreement with the simulation result discussed in previous section. For comparison, a plot of merged experimental and simulational resistivity results is shown in Figure 3.14. The lower level of resistivity from the simulation compared to the experimental result may be ascribed to ideal dispersion of the AgNW in the matrix and fixed 200-aspect ratio of AgNW in contrast to the real experiment where individual nanowire has size distribution [74].
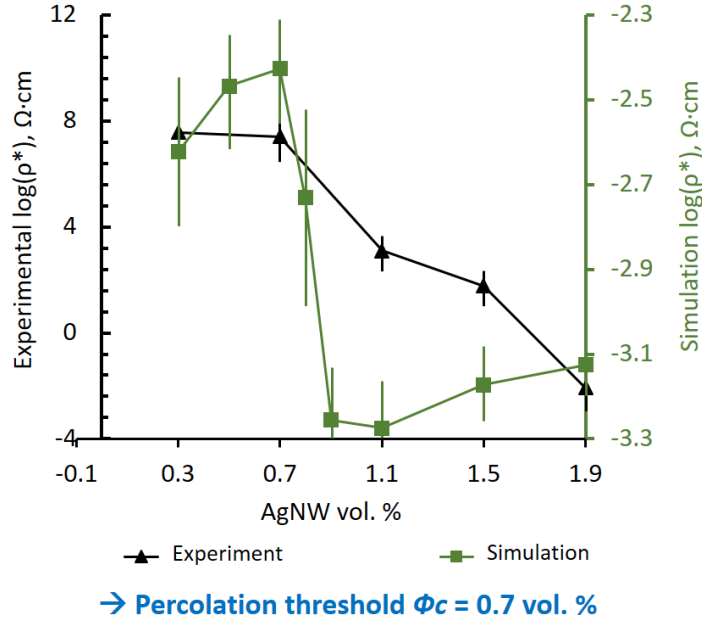
Figure 3.14   Plot of merged experimental and simulational electrical resistivity results with respect to various AgNW vol. %.

The suppressed percolation threshold of 0.7 vol. % and the superior electronic conductivity (8.18×10^{-3} Ω·cm) compared to other reports of AgNW composite [31], [74] suggest an excellent harmony of AgNW filler and CMC matrix for generating a conductive nano-composite.

3.3.2. Confirmation of Power-Law

In a composite which has conductor and insulator phases, the electrical conduction behavior is approximated by a power-law [75]. The power-law can be mathematically represented by an equation below [31].

$$\sigma \approx \left[\frac{(\Phi - \Phi c)}{\Phi c} \right]^{\alpha} \qquad (6)$$

where σ is electronic conductivity, Φc is percolation threshold, Φ is filler volume fraction, and α is critical exponent. As mentioned earlier, percolation can be formed by, (i) a mechanical contact between the conductive fillers or (ii) electron tunneling effect. When the critical exponent α is between 1.1 to 1.3 the percolation network is known to be two-

dimensional (2D) percolation while the α in the range of 1.6 to 2 is 3D percolation [76]. Figure 3.15 shows power law-behavior plot of our AgNW/CMC conductive nano-composite.
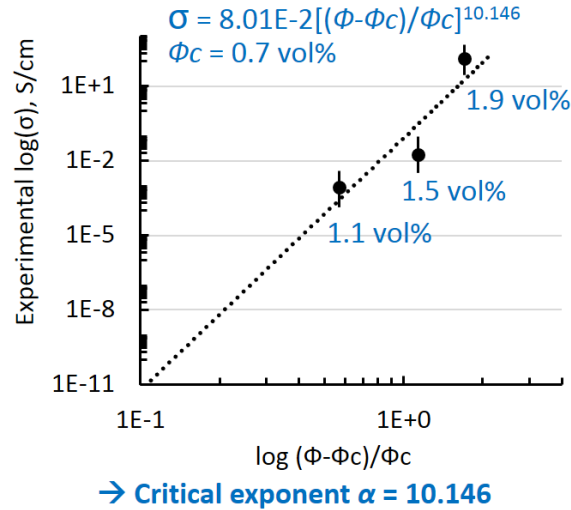
Figure 3.15   Plot of power-law behavior of AgNW/CMC nano-composite.

The percolation threshold Φ_c of 0.7 vol.% and conductivities of the 1.1, 1.5, 1.9 AgNW vol. % nano-composites and a spreadsheet software (Microsoft Excel) was used to find critical exponent of the nano-composite. From the best-fit straight line the critical exponent was found to be 10.146 which indicates that tunneling effect is a dominant charge transport mechanism [75]. Tunneling effect is a main conductivity mechanism of composites made of conductive fillers embedded in insulative matrix [77]. Due to the thin insulative layer surrounding the conductive fillers, the fillers conduct electrons by tunneling effect rather than through their mechanical contacts. It has been reported that the higher volume concentration of the conducive fillers decreases the electron-tunneling distance between the fillers. And the conductive fillers neighboring within the tunneling distance form "clusters". The clusters then form the percolation network enabling electric current to flow through the composite [78].

3.3.3. 3D Printing of AgNW/CMC Composite

Using our paste 3D printing system, 3D printing of AgNW/CMC nano-composite was performed. Three layers of AgNW/CMC paste was printed with each square-shaped layer size of 2×2 cm^2. Each layer height was set 0.5 mm which we found to be most effective to stick the extruded paste on the bed or preceding layer with the nozzle physically pressing the extruded material while printing. A 0.84 mm nozzle was used to extrude the paste with a 0.7 mm/s print head movements speed and 0.0002 ml/s extrusion flow rate. The slow head movement speed was required to wait the high viscosity paste to be extruded. Heated printing bed's temperature set to 70 °C to avoid possible distortion of the printed object during drying process which can lead to a twists or detachment of the part from the printing bed. As shown in Figure 3.16, Two different object infill fractions (100 % and 70 %) were used to print the AgNW/CMC paste.
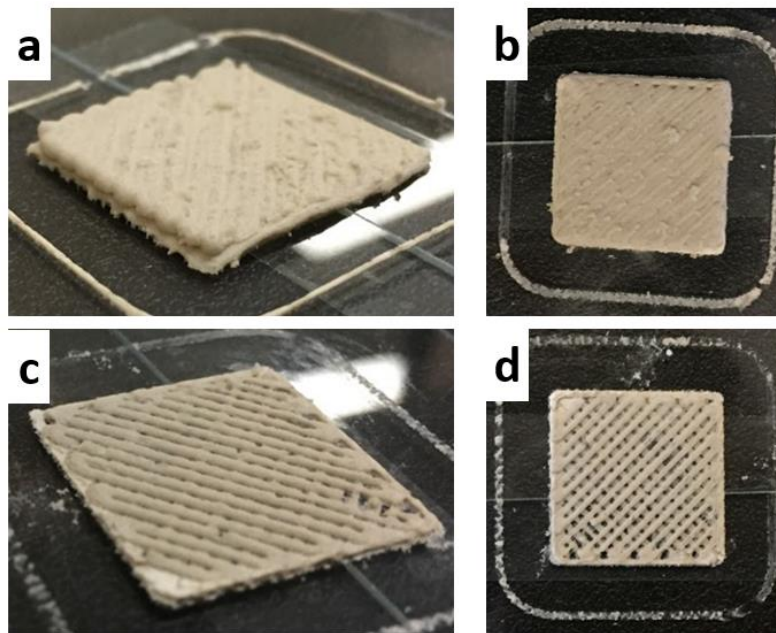
Figure 3.16 **Photographs of 3D printed AgNW/CMC. (a) Isometric view, (b) top view of part with 100 % infill, (c) isometric view, and (d) top view of part with 70 % infill.**

In both designs, no buckling from 1st layer was observed and successful layer stacking capability was demonstrated with our AgNW/CMC composite.

Chapter 4

3D Printed Lithium Polymer Battery

4.1. Introduction

In this chapter, fabrication of 3D printed battery utilized by our conductive AgNW/CMC nano-composite is explained. Planar battery has a basic structure composed of stacked three layers; cathode, anode and electrolyte in between. Studies were done on cathode and anode active materials and their combination with eco-friendly CMC binder was verified.

Among many kinds of batteries, a lithium battery was chosen in this study. Growing demand of lithium for battery application proves advantages of using lithium. Lithium can have the high cell potential compared to other battery materials as lithium has lowest reduction potential, in order words, lithium has tendency to receive electrons and thus gets reduced easily. Also, lithium is the 3rd lightest material in the world which allows lithium battery to have a high specific capacity (mAh g^{-1}) and a great power density [79]. During a discharging stage of a lithium battery, anode undergoes oxidation (loss of electrons) where the lithium materials ($Li_4Ti_5O_{12}$ in our research) gets deintercalated from anode to release electrons and create positive lithium ions. In this process, the lithium cations flow through an ion-permittive electrolyte to the cathode ($LiFePO_4$ in our research) while the electrons flow through an outer circuit for powering to cathode rather than flowing through the insulative electrolyte. As a result, the cathode undergoes reduction (gain of electrons) where the lithium ions meet the electrons and get intercalated. Reversely, in a charging stage of a battery, cathode lithium material undergoes oxidation process (loss of electrons) and release of lithium cations which now flow to anode via electrolyte. And the created electrons flow from the cathode through an outer charging circuit to the anode [80]. Figure 4.1 shows a working mechanism of a lithium battery at a discharging stage [81].
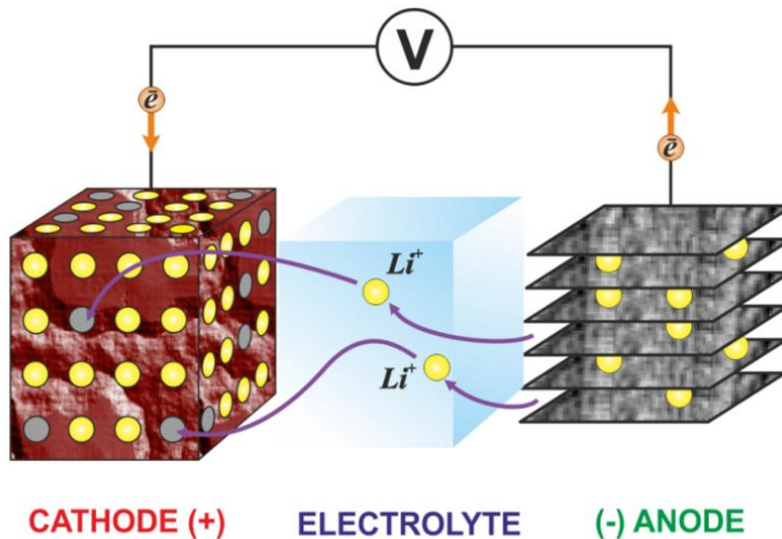
Figure 4.1 **Lithium battery working mechanism at discharging stage [81]. Reprinted with permission.**

In order to 3D print each battery active layer, extrudable cathode and anode pastes were formulated with AgNW/CMC to have high viscosity and thixotropism. Viscosity measurement was performed to confirm rheology behavior (shear-thinning) of the paste. On the other hand, PEO-LiX solid polymer electrolyte was adopted in this study. Solid polymer electrolyte is rising as a safer alternative to conventional liquid electrolytes which can cause internal short-circuit and electrolyte leakage [82]. Ionic conductivity of the fabricated electrolyte was confirmed by an impedance analysis. In later section, fabrication process is explained including a demonstration of consecutive 3D printing of anode, electrolyte, cathode layers, battery packaging, and performance characterization of the battery.

4.2. AgNW-Based Lithium Battery Electrodes

4.2.1. Introduction to Cathode and Anode Active Materials

For cathode and anode fabrication, lithium iron phosphate ($LiFePO_4$, LFP) and lithium titanate ($Li_4Ti_5O_{12}$, LTO) active materials were respectively chosen. LFP is one of the most popularly used cathode material for commercial lithium batteries by beating other lithium materials with its low cost and sufficient capacity. It has brought attentions due to

its advantages such as low cost, stable charge/discharge potential at 3.4 V vs. Li [83], environmental-friendly, high thermal stability, relatively large theoretical specific capacity (170 mAh g^{-1}) [53] and long term cycling capacity reliability [84], [85].

Graphite has been a governing material for anode of lithium battery in the market. It has a low cost, abundancy, high specific capacity (370 mAh g^{-1}) [86], low deintercalation potential of ~0.1 V [79]. However, there are disadvantages of using graphite due to a large volume change (10 %) during charge/discharge cycles [79] and a passivation layer formation on the surface of graphite which increases internal resistance of a battery [87]. LTO is a safer alternative to graphite due to its zero-strain intercalation mechanism, in other words, LTO can have only 0.2 % of volume change during charge/discharge [79]. LTO has stable charge/discharge potential at 1.5 V vs. Li and has theoretical specific capacity of 175 mAh g^{-1} [83].

Regardless of its attractiveness, however, both of LFP and LTO have inferior electronic conductivity. Use of these materials been challenging for their low electronic conductivity ~10^{-9} S/cm for LFP and ~10^{-13} S/cm for LTO respectively [79], [88]. Charge/discharge rate capability is mainly affected by the electronic conductivity of the electrodes. The better conductivity allows faster charging/discharging rate for a battery [89]. Substantial efforts were made to increase the conductivity of LFP by cationic doping [90], carbon coating [91], or mixture with conductive nano-carbon in cathode [92], [93]. For LTO, methods of size reduction of LTO particle to reduce diffusion length of Li+ ion and electrons [94] and cation doping have been investigated [95].

In this research, we investigate fabrication of conductive LFP and LTO electrodes facilitated with addition of highly conductive AgNW fillers to optimize the lithium battery performance.

4.2.2. Preparation of 3D Printable Electrode Paste

3D printable cathode and anode pastes are fabricated as composition shown in Table 4.1. Pastes were carefully designed to acquire 3D printability (high viscosity by CMC), good electronic conductivity (by AgNW), and high lithium active material loading for both the pastes. They were designed to have high filler concentration by including

content of the solid particles (active material, CMC and AgNW) of 40 % in de-ionized (DI) water to minimize inevitable volume shrinkage of printed paste upon drying.

Table 4.1   Prepared cathode and anode composite paste

	vol. % Active Material	vol. % CMC	vol. % AgNW	wt. % Solid Particles
Cathode	78.1	20	1.9	40
Anode	78.1	20	1.9	40

For volume content calculation, densities of 3.6 g/cm^3 was used for LFP particle [96] and 3.539 g/cm^3 were used for LTO [53]. To fabricate 5 g of cathode paste (40 wt. % solids), AgNW (0.121 g) was first dispersed in 3 g of DI water followed by a short (1 min) ultra-sonication with an ultrasonicator (Ultrasonic Bath model 2510, Branson ®). And CMC (0.192 g) was added and stirred until complete dissolve of CMC to form a viscous solution. Cathode active material, 1.687 g of LFP (< 5 um particle size, Sigma Aldrich) particles were then added to the viscous AgNW/CMC mixture and stirred for 20 min. Similarly, for fabrication of 5 g of anode paste (40 wt. % solids), 0.123 g of AgNW, 0.195 g of CMC, and 1.683 g of LTO (< 200 nm particle size, Sigma Aldrich) were dispersed in 3 g of DI water with the same preparation process as LFP paste.
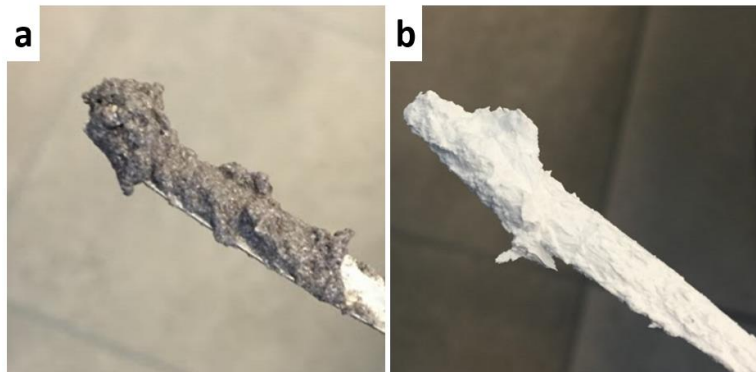
Figure 4.2   Photograph of fabricated (a) cathode (LFP/AgNW/CMC) paste and (b) anode (LTO/AgNW/CMC) paste.

The fabricated showed electronic conductivities of 4.21×10^{-3} S/cm and 1.64×10^{-4} S/cm for cathode and anode paste respectively which are several orders of magnitude more conductive than that of pure LFP and LTO [79], [88]. Also, our pastes' conductivity levels were higher than conductivities of a reported battery electrode pastes which were 4.35×10^{-4} S/cm and 4.76×10^{-6} S/cm for LFP-based and LTO-based electrode pastes [53].

This indicates an effective conductivity enhancing performance even with the low 1.9 vol. % AgNW filler in electrode pastes. However, these conductivities were lower than the conductivity of 1.9 vol. % AgNW concentration AgNW/CMC sample which was 1.22×10^2 S/cm. We believe that the large solid LFP and LTO particles within the electrode paste matrix are interfering even distribution of the AgNW and discouraging percolation network formation in the matrix. The resulting viscous cathode and anode pastes are shown in figure 4.2.

4.3. Polymer Electrolyte

4.3.1. Polymer Electrolyte Background

Polymer electrolyte has been proposed as a replacement for conventional liquid electrolytes. Liquid electrolytes provide higher ionic conductivity and lower production cost compared to the polymer electrolytes [97]. However, battery cells made of the liquid electrolyte can suffer corrosion, toxicity, electrolyte leakage, and internal short-circuit which can lead to cell combustion [98].

Poly(ethylene oxide) (PEO) is a semicrystal polymer and it is one of the widely used polymer electrolyte. But the pure PEO shows poor ionic conductivity in the order of 10^{-8} S/cm due to its high crystallinity at an ambient temperature [97], [98]. For lithium battery, studies have demonstrated increased ionic conductivity up to the range of 10^{-4} S/cm with addition of lithium salt (LiX, X = ClO_4^-, BF_4^-, etc.) and nano-scale inorganic ceramic fillers [99], [100]. Dissolution of the lithium salt is enabled in PEO matrix by chains of PEO surrounding Li+ cations and blocking X- anions [101]. The dissolved cations and anions become mobile in PEO matrix and hop in between PEO chains (Figure 4.3) which, in turn, increase ionic conductivity of the electrolyte [97].
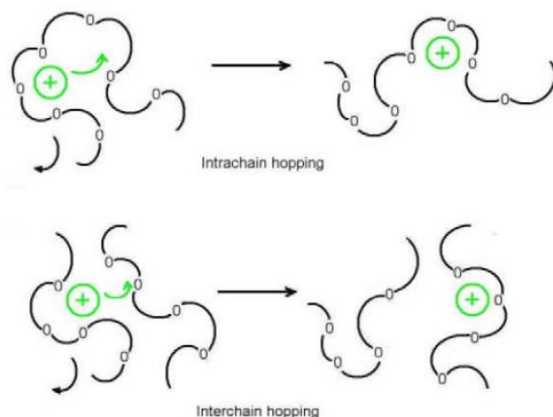
Figure 4.3   Mobility of cations in PEO polymer chains [97]. Reprinted with permission.

Even with the additional lithium salt, PEO matrix favors to be at crystalline phase and only transform to an amorphous phase and become ionic conductive at an elevated temperature over 60 °C [101]. The ceramic fillers have been used in PEO-LiX composite polymer electrolyte and shown to effectively reduce crystallinity of the PEO matrix and increase amorphous regions [99], [100]. The composite electrolytes of PEO-LiX with ceramic fillers were able to achieve useful level of ionic conductivity (10^{-4} S/cm) at a room temperature [101].

4.3.2. Preparation of Polymer Electrolyte and Ionic Conductivity Measurement

In this research, PEO-based electrolyte including $LiClO_4$ (battery grade, Sigma Aldrich) lithium salt and TiO_2 (< 25 nm particle size, Sigma Aldrich) ceramic filler was chosen. PEO is a high molecular weight polymer (M_v ~ 900,000, Sigma Aldrich) implying high viscosity upon dissolution by acetonitrile solvent (Sigma Aldrich) which is suitable for our extrusion platform. For the electrolyte composition, [EO]/[Li] molar ratio of 8 and TiO_2 load of 10 wt. % was chosen as the ratio was studied to have highest ionic conductivity [99], [103], [104]. A complete composition weight ratio is shown in Table 4.2.

Table 4.2   Polymer electrolyte composition ratio

wt. %, PEO	wt. %, LiClO$_4$	wt. %, TiO$_2$
89.2	1.8	9.0

For the PEO-based polymer electrolyte fabrication, a solvent acetonitrile (Sigma Aldrich) was used for particle dispersion. As can be seen from Figure 4.4, $LiClO_4$ and TiO_2 particles were first dispersed by 300 RPM magnet-stirring in acetonitrile for 30 min while maintaining heating temperature at 60 °C. Then relative amount of PEO particles were added to the solution and kept stirred for 3 h until full dissolution of PEO and viscous liquid formation. To carry out impedance analysis on the fabricated electrolyte, the sticky electrolyte was poured on a stainless disk and vacuum dried at 60 °C for 24 h. The dried membrane with thickness of (0.24 mm) was sandwiched with another stainless disk and impedance analysis was performed by measuring impedances with a sweeping frequency from 20 Hz to 2 MHz by a LCR meter (E4980A High Precision LCR Meter, Agilent Technologies).

Magnet-stir LiClO₄ and TiO₂ in Acetonitrile → **Add PEO and keep stirring, viscous liquid formation** → **Impedance measurement with LCR meter**
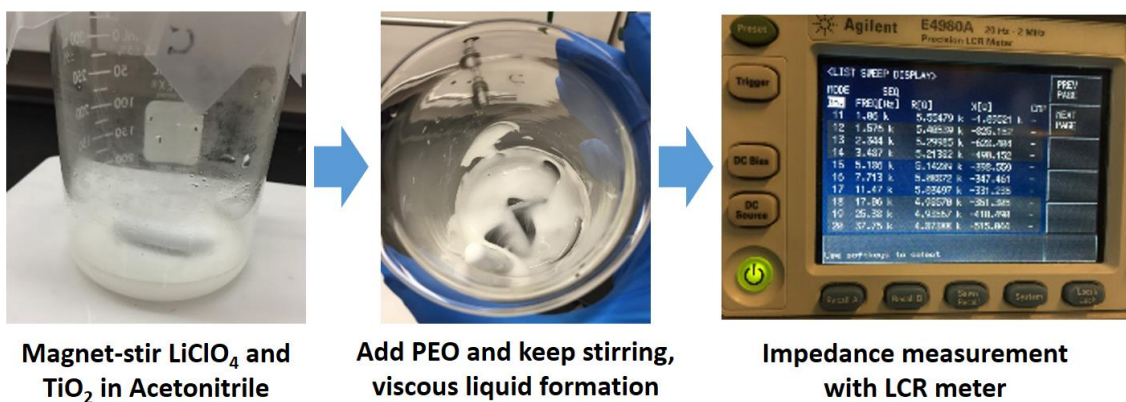
Figure 4.4   Fabrication steps of PEO-LiClO₄-TiO₂ polymer electrolyte.

To calculate an ionic conductivity of the electrolyte, a Nyquist plot had to be plotted as shown in Figure 4.5. Nyquist plot in a shape of slanted line at lower frequency followed by a large semicircle at high frequency was observed as expected [100], [105]. This impedance characteristic of PEO-based electrolyte comes from combined effect by a capacitance of stainless steel electrode in series with a parallel combination of bulk ionic resistance of the electrolyte and electrolyte capacitance [106]. Intercept of the semicircle at high frequency end and the real axis (Z') gives a bulk resistance of the electrolyte [106]. By extending a trend line of the semicircle to intercept the real axis, we can approximate a bulk resistance of the electrolyte to 85.86 Ω.
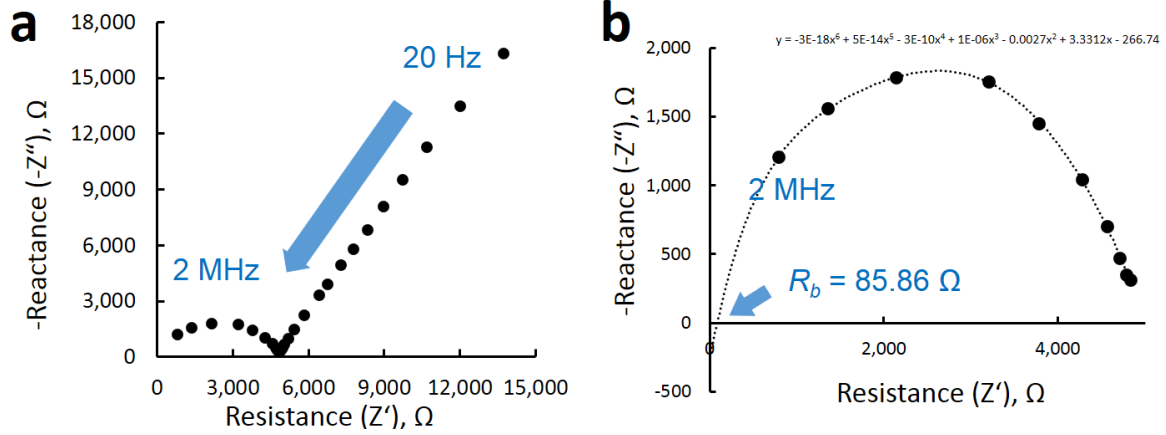
Figure 4.5 **Nyquist plot of PEO-LiClO$_4$-TiO$_2$ electrolyte.**

Ionic conductivity can be calculated using a following equation with the bulk resistance of the electrolyte [107], [108].

$$\sigma = \frac{t}{A \times R_b} \; S\,cm^{-1} = \mathbf{1.83 \times 10^{-4} \; S\,cm^{-1}} \tag{7}$$

where t is a thickness of the electrolyte (0.24 mm), A is a cross-sectional area of the sandwiching stainless disk (1.53 mm^2), and R_b is a bulk resistance of the electrolyte (85.86 Ω). The demonstrated ionic conductivity of our electrolyte agrees with other established researches based on PEO-LiClO$_4$ electrolyte and falls in an useful ionic conductivity level [99], [100], [101].

4.4. 3D Printable Battery

4.4.1. Rheology of Paste and 3D Printability

Electrode pastes must have a great 3D printability, in other words, have an ability to be stacked layer-by-layer without layer buckling. Rheology of the anode paste (LTO/AgNW/CMC) was studied by measuring its viscosity at different shear rates with a viscometer (microVISC™, RheoSense). As can be seen from Figure 4.6, the anode paste demonstrated a strong shear-thinning behavior.

45
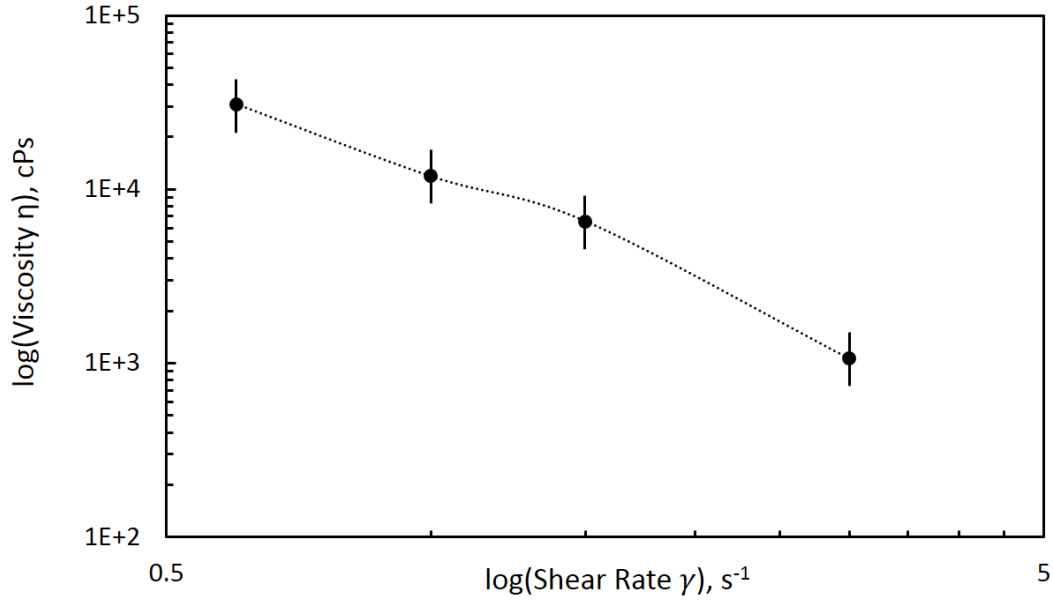
Figure 4.6   Shear-thinning behavior of anode paste.

By increasing shear rate from 0.6 s^{-1} to 3 s^{-1}, viscosity of the paste dropped from 30,832 cps (viscosity level of hot fudge) to 1,063 cps (viscosity level of detergent) [39]. Full viscosity data is shown in Table 4.3.

Table 4.3   Viscosity table of anode paste

Shear Rate γ, s^{-1}	Viscosity η, cPs (mPa s)	Shear Stress τ, Pa
0.6	30,832	11.81
1	11,894	3.19
1.5	6,543	9.78
3	1,063	18.36

Shear rate at the extrusion nozzle can be calculated by using following equation [109].

$$\gamma = \frac{4 \cdot Q}{\pi \cdot R_n^{\,3}} \quad (8)$$

where γ is shear rate (s^{-1}) in the nozzle, Q is extrusion flow rate (0.0002 ml/s or 0.2 mm³/s), and R_n is inner radius of nozzle (0.42 mm). The calculated shear rate for extruding LTO paste was 1.72 s^{-1} which means the viscosity of the paste was around 6,000 cps during extrusion.

A quantitative analysis was also done with Ostwald-de-Waele equation (Power Law) as shown in below equation [37].

$$\tau = \kappa(\gamma)^n \quad (9)$$

where τ is shear stress (Pa), κ is consistency index (Pa s^n), γ is shear rate (s^{-1}), and n is flow behavior index. By using this formula along with given shear rate and shear stress values, we found the flow index n to be 0.2745 which is close to 0 and it indicates the anode paste demonstrates a strong pseudo-plastic (shear-thinning) behavior [37]. This phenomenon implies that the significant decrease of viscosity at higher shear rate allows easier extrusion through narrow printing nozzles (inner diameter of 0.84 mm to 1.54 mm) and the bumped up viscosity after extrusion (no longer shear application) lets the paste to stay in shape and not be spread on the printing bed (Figure 4.7 (a)).

Unfortunately for cathode paste, viscosity measurement was unavailable due to large size of LFP particles which may block a paste flow channel of the viscometer. However, the fabricated cathode paste was also easy to extrude and maintained filamentary shape after extrusion (Figure 4.7 (b)).
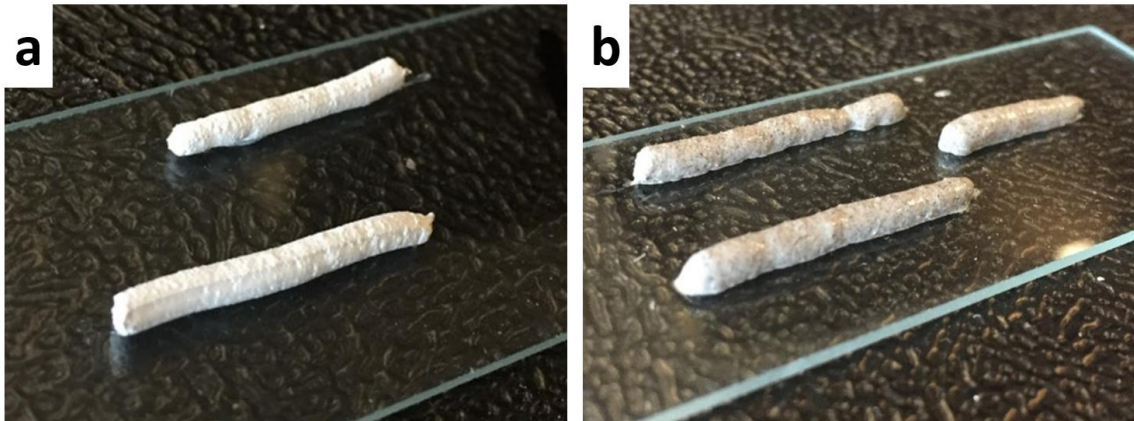
Figure 4.7   Photographs of (a) extruded anode paste and (b) cathode paste.

4.4.2. 3D Printing of Battery

Our 3D printed battery has a three-layer stacked structure, in which, first layer is anode, second layer is electrolyte followed by a third layer of cathode. Each layer was 2 × 2 cm^2 square-shaped. The anode paste was printed on a copper sheet which is a current collector for anode of the battery. A 0.84 mm-nozzle was used to print the anode paste with a slow print head movement speed of 0.7 mm/s and extrusion rate of 0.0002 ml/s. Two layers were printed with each layer-height of 0.5 mm. The anode layer with a thickness of 0.8 mm was achieved upon 15 min drying with a heated printing bed's temperature set to 70 °C. Printing the viscous electrolyte solution, the same printing parameter was used and a single layer of the electrolyte was printed. The printed sample was vacuum dried at 60 °C for 24 h to remove possible moisture from the electrolyte. On the other hand, due to its larger LFP particles clogging the 0.84-mm nozzle, a 1.54 mm-nozzle and extrusion rate of 0.00083 ml/s were used to print the cathode paste. The print head movement speed had to be increased to 1.2 mm/s as more paste was extruded with a larger nozzle. Also only a single layer of cathode paste was printed with a layer-height of 1 mm. On top of the non-dried cathode layer, an aluminum sheet was placed as a current collector for cathode and the complete three-layer sample was dried in vacuum oven at 60 °C for 24 h. Figure 4.8 demonstrates a 3D printing process of the battery.

1st Anode Layer   2nd Electrolyte Layer   3rd Cathode Layer
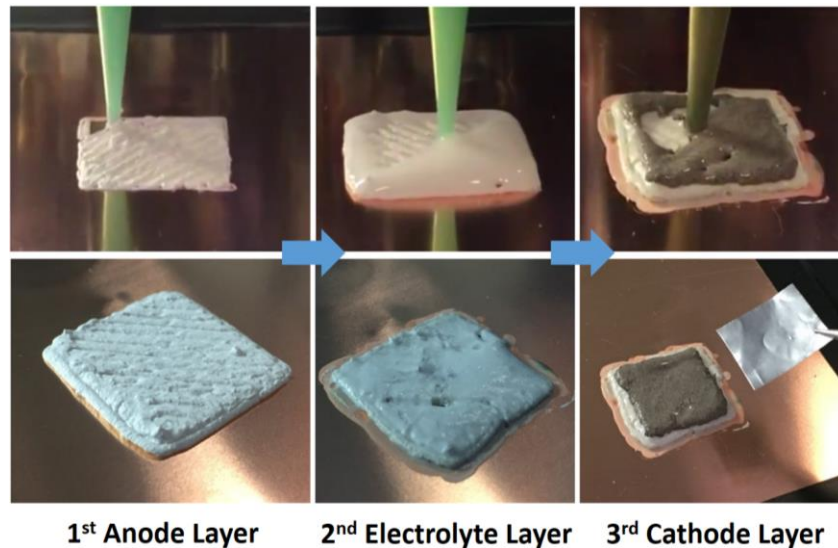
Figure 4.8   **3D printing process of consecutive anode, electrolyte, and cathode layers**

Upon drying of the printed battery, battery cell packaging was performed by attaching nickel tab to anode and aluminum tab on the cathode with an electrical tape. Then, an aluminum-laminated pouch cell case was wrapped around the battery and sealed with a heat iron in order to isolate the battery from ambient environment. The battery packaging process is shown in Figure 4.10.
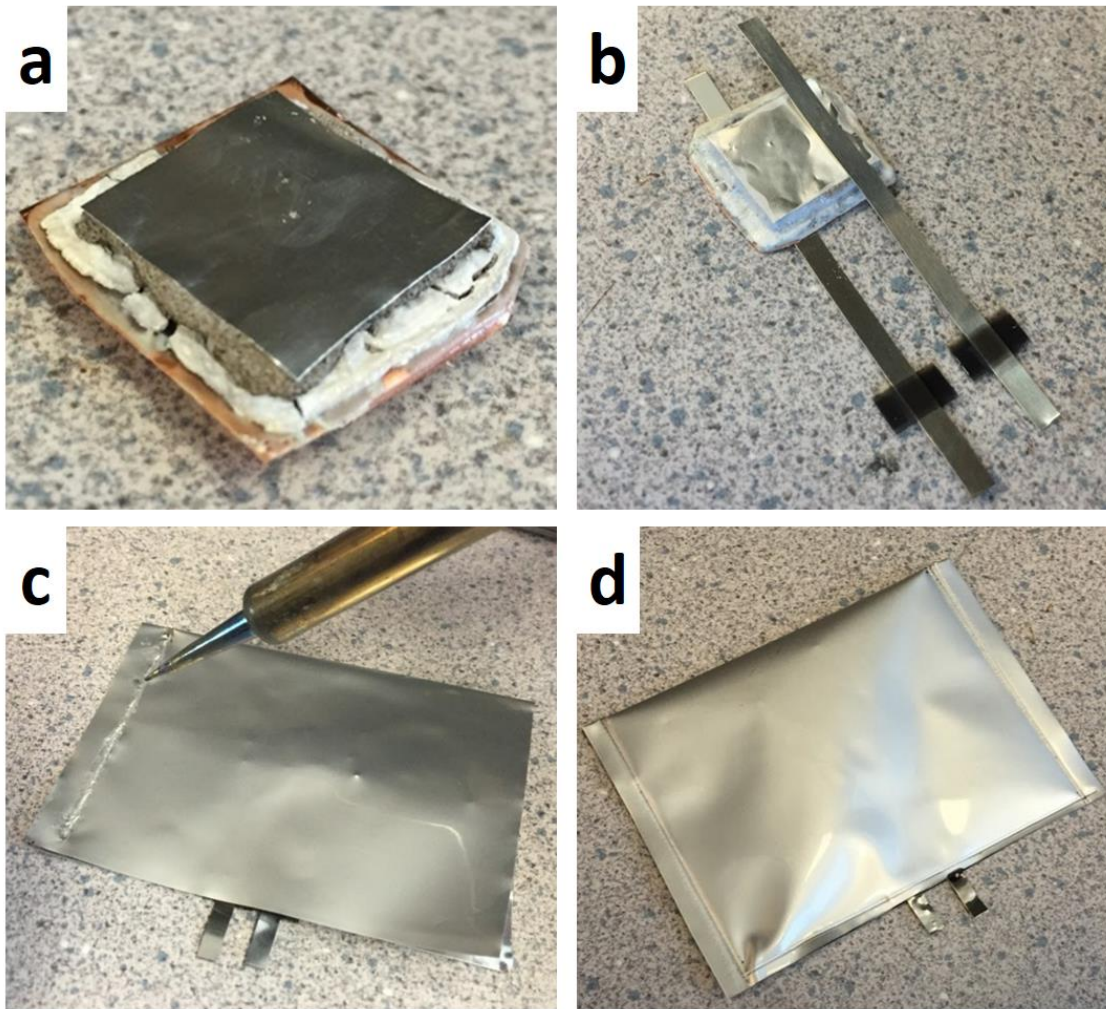
Figure 4.9   **Photographs of (a) completed 3D printed battery, (b) conductive tab attachment on electrodes, (c) pouch cell sealing with heat iron, and (d) completed package of battery.**

4.5. Performance Demonstration of Battery

Constant voltage (CV) charging was performed to see charging characteristic of the battery. Supply voltage of 2 V was applied to the battery and cell voltage was measured every 5 min and battery's voltage profile during charging is shown in Figure 4.10.
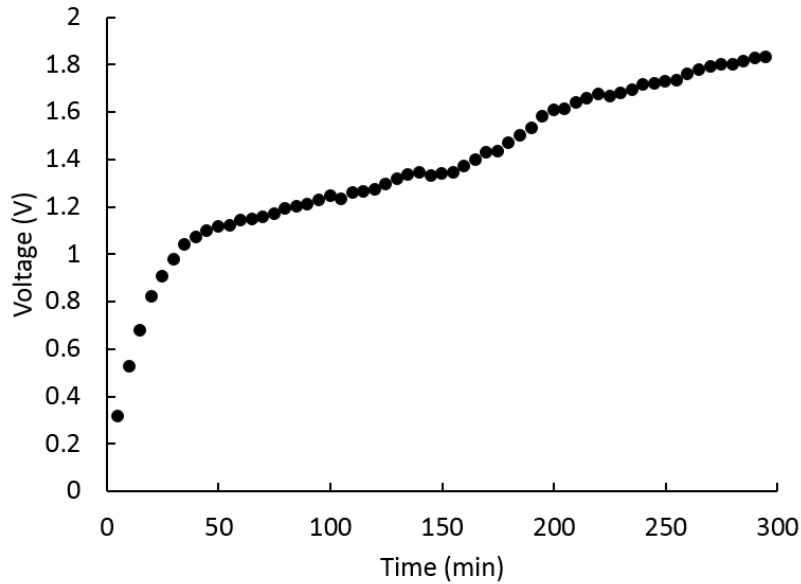
Figure 4.10   Voltage profile of battery during constant voltage charging.

After charging the battery under the discharged state of 0.32 V, the open circuit voltage of the battery increased to about 1.2 V after 1 h 25 min and around 1.8 V after 4h 35 min. Voltage of a cell is determined by a potential difference between the cathode and anode. Potential for LFP range between 3.2 and 3.5 V while for LFP it is about 1.55 V which leads to a potential of LFP/LTO full cell to be around 1.8 V [53], [83], [87]. Demonstrated cell voltage of our 3D printed battery showed a good agreement with reported cell voltages of LFP/LTO batteries which are in the range of 1.5 ~ 1.8 V [110].
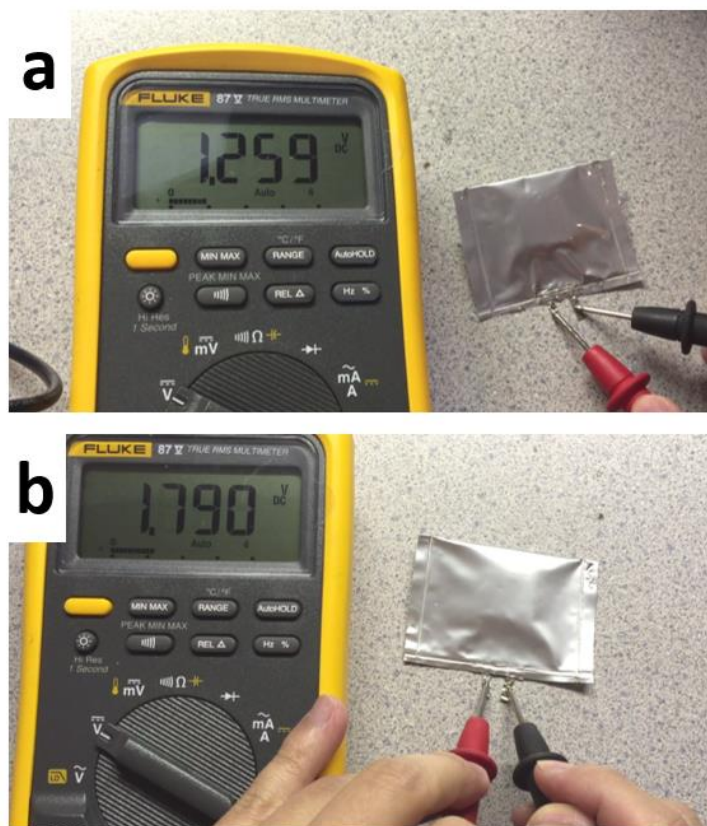
Figure 4.11   Open circuit voltage measurement from the 3D printed battery (a) after 2 h of charging and (b) after 4 h 35 min of charging.

Although constant current charging and an exact battery capacity measurement were unavailable, capacity can be approximated with active material weight and the active material's specific capacity. The mass loading of active materials in the battery was measured to be 0.17 g while the total weight of the fabricated battery was 1.16 g including metal current collectors. Specific capacity (mAh g^{-1}) of LFP/LTO full cell is reported to be about 110 mAh g^{-1} [1], [83] suggesting our 3D printed battery capacity around 18.7 mAh.

Chapter 5

Conclusion and Future Work

5.1. Conclusion

In this thesis, 3D printable conductive nano-composite has been developed. Highly conductive cylinder-shaped AgNW was used as a conductive filler in the eco-friendly CMC matrix due to its strong thixotropic rheology which is advantageous for 3D printing application. Also, novel and low-cost paste 3D printing platform was established by a simple integration of a commercial delta 3D printer and a paste extruder. Finally, battery electrode pastes were formulated based on AgNW/CMC composite for the demonstration of 3D printed battery. The key findings from this research are summarized as below:

1. Design and evaluation of conductive nano-composite:
    (a) AgNW is used as a conductive filler. AgNW has high-aspect ratio shape with each AgNW having a metallic conductivity. It can benefit when creating a conductive nano-composite compared to other spherical or platelet nanoparticles.
    (b) CMC is used as a matrix. CMC is a water-soluble and nature-friendly material proposing a toxic-free process. Also, making a composite with CMC is allows easy disposal of the composite after use by returning filler materials by a pyrolysis of the CMC [84].
    (c) A simulational study using a composite modeling software and an electrical conductance simulation tool estimated a percolation threshold.
    (d) AgNW/CMC nano-composites were fabricated in various concentration of AgNW to experimentally find a percolation threshold of the nano-composite.
    (e) From both simulational and experimental studies, the discovered percolation threshold was only 0.7 vol. % of AgNW which was significantly lower than other composites using low-aspect ratio conductive fillers.
    (f) High conductivity of 1.22×10^2 S/cm was achieved from the AgNW/CMC composite with low 1.9 vol. % loading of AgNW.
2. Demonstration of 3D printed battery using conductive nano-composite:

(a) Utilizing the high conductivity of the AgNW/CMC composite, battery electrode pastes were designed and printed with the paste 3D printing platform.

(b) PEO-based electrolyte is fabricated and evaluated.

(c) Rheology study proved that the thixotropism of the fabricated electrode pastes aided by the CMC's strong thixotropic rheology, which allowed the 3D printing of the CMC-based electrode pastes.

(d) Anode, electrolyte, and cathode pastes were consecutively printed to form a typical three-layer lithium battery. And the fabricated battery's performance is demonstrated.

5.2. Future work

Newly proposed 3D printing platform and AgNW/CMC nano-composite's thixotropic property shows a practical printability. Additionally, there are few more items to be improved for better 3D printing quality.

5.2.1. Advancement of Printed Part Quality

Despite the easy and low-cost 3D printing manufacturing process with the CMC-based nano-composite paste, printed parts showed minor cracking or detachment from the printing bed upon drying which affected the quality of the final product. CMC naturally undergoes a significant volume change which can create such deformations. It can be solved by increasing the fraction of solid filler content and reducing solvent amount to minimize the volume shrinkage. Another popular method to enhance binding is to add a little amount styrene-butadiene rubber (SBR) [111].

5.2.2. Variation of 3D Printed Battery Designs

Conventional battery electrodes are commonly made by electrode slurry casting and blading on current collectors which requires large electrode area and restricts producing various shape of electrodes. Due to the unique manufacturing process of the 3D printing technology, printed objects can have multiple number of layers being stacked. Utilizing this technique to the battery's 3D printing process, cathode, electrolyte, and anode layers can be stacked in alternating way and form a standing battery with a high

areal capacity (mAh/cm^2). Also with the 3D printing method, battery shapes are not limited to the conventional coin cell, cylinder cell or planar pouch cell. Batteries can be fabricated in any shapes to fully utilize confined area especially in portable electronic devices.

References

[1]   K. Fu, Y. Wang , C. Yan, Y. Yao, Y. Chen, J. Dai, and S. Lacey, "Graphene Oxide-
        Based Electrode Inks for 3D-Printed Lithium-Ion Batteries," *Adv. Mater.,* vol. 28,
        p. 2587–2594, 2016.

[2]   K. Markstedt, A. Mantas, I. Tournier, H. M. Ávila, D. Hägg, and P. Gatenholm ,
        "3D Bioprinting Human Chondrocytes with Nanocellulose−Alginate Bioink for
        Cartilage Tissue Engineering Applications," *Biomacromolecules,* vol. 16, pp.
        1489-1496, 2015.

[3]   T. T. Wohlers, "Wohlers report 2016: 3D printing and additive manufacturing state
        of the industry," Wohlers Associates, Fort Collins, CO, 2016.

[4]   "3D Printing Market (Technologies, Materials, Applications and Geography) -
        Global Opportunity Analysis and Forecast-2013-2020," Research and Markets,
        Dublin 8, Ireland, 2014.

[5]   Alan Earls and Vinod Baya, "The road ahead for 3-D printers," PwC Technology
        Forecast, UK, 2014.

[6]   B. C. Gross, J. L. Erkal, S. Y. Lockwood, C. Chen, and D. M. Spence, "Evaluation
        of 3D Printing and Its Potential Impact on Biotechnology and the Chemical
        Sciences," *Anal. Chem.,* vol. 86, p. 3240−3253, 2014.

[7]   F. Rengier, A. Mehndiratta, H. von Tengg-Kobligk, C. M. Zechmann, R.
        Unterhinninghofen, H.-U. Kauczor, and F. L. Giesel, "3D printing based on
        imaging data: review of medical applications," *Int. J. CARS,* vol. 5, pp. 335-341,
        2010.

[8]   F. Fischer, "Thermoplastics: the best choice for 3d printing," Startasys Inc., Eden Prairie, MN, 2011.

[9]   "Conductive PLA," Proto-pasta, [Online]. Available: https://www.proto-pasta.com/pages/conductive-pla. [Accessed 6 June 2016].

[10]   "Conductive Graphene Filament," Black Magic 3D, [Online]. Available: http://www.blackmagic3d.com/Conductive-p/grphn-175.htm. [Accessed 6 June 2016].

[11]   W. Xu, Q. Xu, Q. Huang, R. Tan, W. Shen, W. Song, "Electrically conductive silver nanowires-filled methylcellulose composite transparent films with high mechanical properties," *Mater. Lett.,* vol. 152, pp. 173-176, 2015.

[12]   T. Inui, H. Koga, M. Nogi, N. Komoda and K. Suganuma, "High-Dielectric Paper Composite Consisting of Cellulose Nanofiber and Silver Nanowire," in *14th IEEE International Conference on Nanotechnology*, Toronto, Canada, 2014.

[13]   D. Hawkins, "Addition of chelated trivalent cations to solutions of the polymer sodium carboxymethylcellulose (CMC)," M.Sc. Thesis Dissertation, Dept. of Chem., Rochester Institute of Technology, Rochester, New York, 1999.

[14]   S. Bijadi, "Feasibility of Additive Manufacturing Method for Developing Stretchable and Flexible Embedded Circuits," M.Sc. Thesis Dissertation, Dept. of Mech. Eng., University of Minnesota, Minneapolis, 2014.

[15]   S. Padmanabhan, "Lithium-Ion Battery Market is Expected to Reach $46.21 Billion, Worldwide, by 2022," PR Newswire Association LLC., 2016. [Online]. Available: http://www.prnewswire.com/news-releases/lithium-ion-battery-market-is-expected-to-reach-4621-billion-worldwide-by-2022-575386231.html. [Accessed 13th June 2016].

[16]   A. P. Alivisatos, "Semiconductor clusters, nanocrystals, and quantum dots," *Science,* vol. 271, pp. 933-937, 1996.

[17]   P. Buffat and J. P. Borel, "Size effect on the melting temperature of gold particles," *Phys. Rev. A,* vol. 13, pp. 2287-2297, 1976.

[18]   C. Wang, Z.-X. Guo, S. Fu, W. Wu, and D. Zhu, "Polymers containing fullerene or carbon nanotube structures," *Prog. Polym. Sci.,* vol. 29, pp. 1079-1141, 2004.

[19]   R. Sardar, A. M. Funston, P. Mulvaney, and R. W. Murray, "Gold nanoparticles: past, present, and future," *Langmuir,* vol. 25, p. 13840–13851, 2009.

[20]   O. Ivanova, C. Williams, and T. Campbell, "Additive manufacturing (AM) and nanotechnology," *Rapid Prototyping J.,* vol. 19, p. 353–364, 2013.

[21]   I. J. Sanders and T. L. Peeten, Carbon black: production, properties, and uses, New York: Nova Science Publishers Inc. , 2011.

[22]   P. C. Ma, J.-K. Kim, and B. Z. Tang, "Effects of silane functionalization on the properties of carbon nanotube/epoxy nano-composites," *Compos. Sci. Technol.,* vol. 67, p. 2965–2972, 2007.

[23]   Y. Zhu, X. Zhang, J. Zhu, Q. Zhao, Y. Li, W. Li, C. Fan and Q. Huang, "Cytotoxicity of Phenol Red in Toxicity Assays for Carbon Nanoparticles," *Int. J. Mol. Sci.,* vol. 13, p. 12336–12348, 2012.

[24]   K. P. Sau, D. Khastgir, T. K. Chaki, "Electrical conductivity of carbon black and carbon fibre filled silicone rubber composites," *Angew. Makromol. Chem.,* vol. 258, p. 11–17, 1998.

[25] J. Li, P. C. Ma, W. S. Chow, C. K. To, B. Z. Tang, and J.-K. Kim, "Correlations between Percolation Threshold, Dispersion State and Aspect Ratio of Carbon Nanotubes," *Adv. Funct. Mater. ,* vol. 17, p. 3207–3215 , 2007.

[26] O. Koysuren, S. Yesil and G. Bayram, "Effect of Composite Preparation Techniques on Electrical and Mechanical Properties and Morphology of Nylon 6 Based Conductive Polymer Composites," *J. Appl. Polym. Sci.,* vol. 102, p. 2520– 2526, 2006.

[27] J. Sandler, M.S.P. Shaffer, T. Prasse, W. Bauhofer, K. Schulte, and A.H. Windle, "Development of a dispersion process for carbon nanotubes in an epoxy matrix and the resulting electrical properties," *Polym.,* vol. 40, p. 5967–5971, 1999.

[28] A. Sakhaee-Pour, M.T. Ahmadiana, and A. Vafai, "Potential application of single-layered graphene sheet as strain sensor," *Solid State Commun.,* vol. 147, p. 336– 340, 2008.

[29] Y. Sun, B. Mayers, T. Herricks, and Y. Xia, "Polyol Synthesis of Uniform Silver Nanowires: A Plausible Growth Mechanism and the Supporting Evidence," *Nano Lett.,* vol. 7, pp. 955-960, 2003.

[30] F. Xu and Y, Zhu, "Highly Conductive and Stretchable Silver Nanowire Conductors," *Adv. Mater.,* vol. 24, p. 5117–5122, 2012.

[31] S. I. White, R. M. Mutiso, P. M. Vora, D. Jahnke, S. Hsu, J. M. Kikkawa, J. Li, J. E. Fischer, and K. I. Winey, "Electrical Percolation Behavior in Silver Nanowire– Polystyrene Composites: Simulation and Experiment," *Adv. Funct. Mater.,* vol. 20, p. 2709–2716, 2010.

[32] A. A. Wereszczak, D. J. Vuono, H. Wang, and M. K. Ferber, "Properties of Bulk Sintered Silver As a Function of Porosity," Oak Ridge National Laboratory, Oak Ridge, 2012.

[33] D. P. Langley, M. Lagrange, G. Giusti, C. Jiménez, Y. Bréchet, N. D. Nguyenb, and D. Bellet, "Metallic nanowire networks: effects of thermal annealing on electrical resistance," *Nanoscale,* vol. 6, p. 13535–13543, 2014.

[34] D. Hawkins, "Addition of chelated trivalent cations to solutions of the polymer sodium carboxymethylcellulose (CMC)," M.Sc. Thesis Dissertation, Dept. of Chem., Rochester Institute of Technology, Rochester, 1999.

[35] V. Pushpamalar , S.J. Langford , M. Ahmad , and Y.Y. Lim, "Optimization of reaction conditions for preparing carboxymethyl cellulose from sago waste," *Carbohydr. Polym.*, vol. 64, p. 312–318, 2006.

[36] H. Togˇrul and N. Arslan, "Production of carboxymethyl cellulose from sugar beet pulp cellulose and rheological behaviour of carboxymethyl cellulose," *Carbohydr. Polym.,* vol. 54, p. 73–82, 2003.

[37] M. Edali, M. N. Esmail, and G. H. Vatistas, "Rheological Properties of High Concentrations of Carboxymethyl Cellulose Solutions," *J. Appl. Polym. Sci.,* vol. 79, p. 1787–1801, 2001.

[38] A. Benchabane and K. Bekkour, "Rheological properties of carboxymethyl cellulose (CMC) solutions," *Colloid. Polym. Sci.,* vol. 286, p. 1173–1180, 2008.

[39] "Viscosity Charts & Conversion Tables," BASCO, Inc., [Online]. Available: http://bascousa.com/images/advisors/407%20condensed.pdf. [Accessed 15th June 2016].

[40]   S.S. Jeong, N. Böckenfeld, A. Balducci, M. Winter, and S. Passerini, "Natural cellulose as binder for lithium battery electrodes," *J. Power Sources,* vol. 199, p. 331– 335, 2012.

[41]   H. Buqaa, M. Holzapfel, F. Krumeich, C. Veitc, P. Nov´ak, "Study of styrene butadiene rubber and sodium methyl cellulose as binder for negative electrodes in lithium-ion batteries," *J. of Power Sources,* vol. 161, p. 617–622, 2006.

[42]   G.T. Kim, S.S. Jeong, M. Joost, E. Rocca, M. Winter, S. Passerini, and A. Balducci, "Use of natural binders and ionic liquid electrolytes for greener and safer lithium-ion batteries," *J. of Power Sources,* vol. 196, p. 2187–2194, 2011.

[43]   T. Akter and W. S. Kim, "Reversibly Stretchable Transparent Conductive Coatings of Spray-Deposited Silver Nanowires," *ACS Appl. Mater. Interfaces,* vol. 4, p. 1855−1859, 2012.

[44]   T, Campbell, C. Williams, O. Ivanova, and B. Garrett, "Could 3D Printing Change the World? Technologies, Potential, and Implications of Additive Manufacturing," Atlantic Council, Washington, 2011.

[45]   D. Espalin, D. W. Muse, E. MacDonald, and R. B. Wicker, "3D Printing multifunctionality: structures with electronics," *Int. J. Adv. Manuf. Technol.,* vol. 72, pp. 963-978, 2014.

[46]   S. J. Leigh, R. J. Bradley, C. P. Purssell, D. R. Billson, and D. A Hutchins, "A Simplt, Low-Cost Conductive Composite Material for 3D Printing of Electronics Sensors," *Plos One,* vol. 7, p. e49365, 2012.

[47]   A. Tsouknidas, "Friction Induced Wear of Rapid Prototyping Generated Materials: A Review," *Adv. Tribol.,* vol. 2011, p. 746270, 2011.

[48]   R. D. Farahani, K. Chizari and D. Therriault, "Three-dimensional printing of freeform helical microstructures: a review," *Nanoscale,* vol. 6, p. 10470, 2014.

[49]   G. Wu, B. Zhou, Y. Bi, and Y. Zhao, "Selective laser sintering technology for customized fabrication of facial prostheses," *J. Prosthet. Dent.,* vol. 100, pp. 56-60, 2008.

[50]   A. Pîrjan, and D.-M. Petroşanu, "The impact of 3D printing technology on the society and economy," *JISOM,* vol. 7, pp. 360-370, 2013.

[51]   "Rapid Prototyping," Protosys Technologies Pvt. Ltd., [Online]. Available: http://www.protosystech.com/rapid-prototyping.htm. [Accessed 13th June 2016].

[52]   T. J. Ober, D. Foresti, and J. A. Lewis, "Active mixing of complex fluids at the microscale," *Proceedings of the National Academy of Sciences,* vol. 112, p. 12293–12298, 2015.

[53]   K. Sun, T.-S. Wei , B. Y. Ahn, J. Y. Seo, S. J. Dillon, and J. A. Lewis, "3D Printing of Interdigitated Li-Ion Microbattery Architectures," *Adv. Mater.,* vol. 25, p. 4539–4543, 2013.

[54]   L. L. Lebel, B. Aissa, M. A. El Khakani and D. Therriault, "Ultraviolet-Assisted Direct-Write Fabrication of Carbon Nanotube/Polymer Nano-composite Microcoils," *Adv. Mater.,* vol. 22, p. 592–596, 2010.

[55]   W. Li, A. Ghazanfari, M. C. Leu, and R. G. Landers, "Methods of Extrusion on demand for high solids loading ceramic paste in freeform extrusion fabrication," Missouri University of Science and Technology, Rolla.

[56]   K. Markstedt, J. Sundberg, and P. Gatenholm, "3D Bioprinting of Cellulose Structures from an Ionic Liquid," *3D Print. Addit. Manuf.,* vol. 1, pp. 115-121, 2014.

[57]   G. Buckle, "ORION USERS MANUAL," 27 June 2015. [Online]. Available: http://download.seemecnc.com/orion/OrionUserManual-3rdEd.pdf. [Accessed 6 June 2016].

[58]   "Discov3ry - A Universal Paste Extruder For Your Desktop 3D Printer," Structu3r Printing, [Online]. Available: http://www.structur3d.io/discov3ry-products/discov3ry. [Accessed 6 June 2016].

[59]   "Felix 3.1 + Discov3ry Integration Wiki & Discussion Thread," Structur3d 3D Printing, August 2015. [Online]. Available: http://forum.structur3d.io/t/felix-3-1-discov3ry-integration-wiki-discussion-thread/353. [Accessed 6 June 2016].

[60]   "Repetier-Host," Repetier, [Online]. Available: https://www.repetier.com/. [Accessed 7 June 2016].

[61]   "Hydraulic Backpressure," Munckhof, 11 July 2011. [Online]. Available: http://www.munckhof.com/blog/vineyard/hydraulic-backpressure/. [Accessed 8 June 2016].

[62]   N. Hu, Y. Karubea, C. Yan, Z. Masuda, and H. Fukunaga, "Tunneling Effect in a Polymer/Carbon Nanotube Nano-composite Strain Sensor," *Acta Mater.,* vol. 56, pp. 2929-2936, 2008.

[63]   A. B. Oskouyi, U. Sundararaj, and P. Mertiny, "Effect of Temperature on Electrical Resistivity of Carbon Nanotubes and Graphene Nanoplatelets Nano-composites," *J. Nanotechnol. Eng. Med.,* vol. 5, pp. 044501-1, 2014.

[64] T. Tokuno, M. Nogi, M. Karakawa, J. Jiu, T. T. Nge, Y. Aso, and K. Suganuma, "Fabrication of Silver Nanowire Transparent Electrodes at Room Temperature," *Nano Res.,* vol. 4, p. 1215–1222, 2011.

[65] A. Fathi, K. Hatami, and B. P. Grady, "Effect of carbon black structure on low-strain conductivity of polypropylene and low-density polyethylene composites," *Polym. Eng. Sci.*, vol. 52, p. 549–556, 2012.

[66] A. Lonjon, P. Demont, E. Dantras, and C. Lacabanne "Low filled conductive P(VDF-TrFE) composites: Influence of silver particles aspect ratio on percolation threshold from spheres to nanowires," *J. Non-Cryst. Solids,* vol. 358, p. 3074–3078, 2012.

[67] P. Fremerey, A. Jess, and R. Moos, "Why does the Conductivity of a Nickel Catalyst Increase during Sulfidation? An Exemplary Study Using an In Operando Sensor Device," *Sensors,* vol. 15, pp. 27021-27034, 2015.

[68] R. Hill, "Elastic properties of reinforced solids: some theoretical principles," *J. Mech. Phys. Solids,* vol. 11, pp. 357-372, 1963.

[69] M. M. A. Moteleb, "Electrical conductance of some cellulose derivatives," *Polym. Bull.,* vol. 28, pp. 689-695, 1992.

[70] D. Giancoli, Physics for Scientists and Engineers with Modern Physics (4th ed.), Upper Saddle River: Prentice Hall, 1984.

[71] "9004-32-4(Carboxymethyl cellulose) Product Description," ChemicalBook, [Online]. Available: http://us.chemicalbook.com/ChemicalProductProperty_US_CB5209844.aspx. [Accessed 11 June 2016].

[72]   D. Langley, G. Giusti, C. Mayousse, C. Celle, D. Bellet, and J.-P. Simonato, "Flexible transparent conductive materials based on silver nanowire networks: a review," *Nanotechnol.,* vol. 24, p. 452001, 2013.

[73]   S. De, T. M. Higgins, P., E. Lyons, E. M. Doherty, P. N. Nirmalraj, W. J. Blau, J. J. Boland, and J. N. Coleman, "Silver nanowire networks as flexible, transparent, conducting films: extremely high DC to optical conductivity ratios," *ACS Nano,* vol. 3, p. 1767–1774, 2009.

[74]   G. A. Gelves, B. Lin, U. Sundararaj, and J. A. Haber, "Low Electrical Percolation Threshold of Silver and Copper Nanowires in Polystyrene Composites," *Adv. Funct. Mater.,* vol. 16, p. 2423–2430, 2006.

[75]   N. Johner, C. Grimaldi, I. Balberg, and P. Ryser, "Transport exponent in a three-dimensional continuum tunneling-percolation model," *Phys. Rev.,* vol. 77, p. 174204, 2008.

[76]   O. Fesenko, L. Yatsenko, "Nano-composites, Nanophotonics, Nanobiotechnology, and Applications," in *Selected Proceedings of the Second FP7 Conference and International Summer School Nanotechnology*, Bukovel, Ukraine, 2013.

[77]   L. Feng, N.Xie, and J. Zhong, "Carbon Nanofibers and Their Composites: A Review of Synthesizing, Properties and Applications," *Materials*, vol. 7, pp. 3919-3945, 2014.

[78]   A. B. Oskouyi, U. Sundararaj, and P. Mertiny, "Tunneling Conductivity and Piezoresistivity of Composites Containing Randomly Dispersed Conductive Nano-Platelets," *Materials*, vol. 7, pp. 2501-2521, 2014.

[79]   N. Nitta, F. Wu, J. T. Lee, and G. Yushin, "Li-ion battery materials: present and future," *Mater. Today,* vol. 18, pp. 252-264, 2015.

[80]   "How cells work," Johnson Matthey Battery Systems, 2014. [Online]. Available: http://www.jmbatterysystems.com/technology/cells/how-cells-work.   [Accessed 22nd June 2016].

[81]   M. Molenda, M. Świętosławski, and R. Dziembaj, "C/Li2MnSiO4 Nano-composite Cathode Material for Li-Ion Batteries," in *Composites and Their Properties*, Rijeka, Croatia, InTech, 2012, pp. 61-80.

[82]   A. M. Stephan, "Review on gel polymer electrolytes for lithium batteries," *Eur. Polym. J.,* vol. 42, p. 21–42, 2006.

[83]   A. Jaiswal, C. R. Horne, O. Chang, W. Zhang, W. Kong, E. Wang, T. Chern, and M. M. Doeff, "Nanoscale LiFePO4 and Li4Ti5O12 for High Rate Li-ion Batteries," *J. Electrochem. Soc.,* vol. 156, pp. A1041-A1046, 2009.

[84]   S. F. Lux, F. Schappacher, A. Balducci, S. Passerini, and M. Winter, "Low Cost, Environmentally Benign Binders for Lithium-Ion Batteries," *J. Electrochem. Soc.,* vol. 157, pp. A320-A325, 2010.

[85]   "Fine-particle lithium iron phosphate LiFePO4 synthesized by a new low-cost aqueous precipitation technique," *J. Power Sources,* vol. 119–121, p. 247–251, 2003.

[86]   M. Yoshio, H. Wang, K. Fukuda, T. Umeno, T. Abe and Z. Ogumi, "Improvement of natural graphite as a lithium-ion battery anode material, from raw flake to carbon-coated sphere," *J. Mater. Chem.,* vol. 14, p. 1754–1758, 2004.

[87] K. Zaghib, M. Dontigny, A. Guerfi, P. Charest, I. Rodrigues, A. Mauger, and C. M. Julien, " Safe and fast-charging Li-ion battery with long shelf life for power applications," *J. Power Sources,* vol. 196, pp. 3949-3954, 2011.

[88] C.S. Sun, Z. Zhou, Z.G. Xu, D.G.Wang, J.P.Wei, X.K. Bian, and J. Yan, "Improved high-rate charge/discharge performances of LiFePO4/C via V-doping," *J. Power Sources,* vol. 193, p. 841–845, 2009.

[89] H. Park, T. Song, H. Han, and U. Paik, "Electrospun Li4Ti5O12 nanofibers sheathed with conductive TiN/TiOxNy layer as an anode material for high power Li-ion batteries," *J. Power Sources,* vol. 244, pp. 726-730, 2013.

[90] S.-Y. Chung, J. T. Bloking, and Y.-M. Chiang, "Electronically conductive phospho-olivines as lithium storage electrodes," *Nat. Mater.,* vol. 1, pp. 123-128, 2002.

[91] M. Armand, M. Gauthier, J.-F. Magnan, and N. Ravet, "Method for synthesis of carbon-coated redox materials with controlled size". US Patent US 7601318 B2, 13 Oct 2009.

[92] C. Delacourt, P. Poizot, S. Levasseur, and C. Masquelier, "Size Effects on Carbon-Free LiFePO4 Powders," *Electrochem. Solid State Lett.,* vol. 9, pp. A352-A355, 2006.

[93] K.-H. Choi, S.-J. Cho, S.-J. Chun, J. T. Yoo, C. K. Lee, W. Kim, Q. Wu, S.-B. Park, D.-H. Choi, S.-Y. Lee, and S.-Y. Lee, "Heterolayered, One-Dimensional Nanobuilding Block Mat Batteries," *Nano Lett.,* vol. 14, p. 5677−5686, 2014.

[94] L. Wu, S. R. Kan, S. G. Lu, X. J. Zhang, and W. H. Jin, "Effect of Particle Size and Agglomeration of TiO2 on Synthesis and Electrochemical Properties of Li4Ti5O12," *Transactions of Nonferrous Metals Society of China,* vol. 17, pp. s117-s121, 2007.

[95] H. Chen, J. T. Vaughey, A. N. Jansen, D. W. Dees, A. J. Kahaian, T. Goacher, and M. M. Thackeray, "Studies of Mg-Substituted Li4− xMg x Ti5O12 Spinel Electrodes (0≤ x≤ 1) for Lithium Batteries," *J. Electrochem. Soc.,* vol. 148, pp. A102-A104, 2001.

[96] J. Lia, B. L. Armstrong, J. Kiggans, C. Daniel, and D. L. Wood, "Lithium Ion Cell Performance Enhancement Using Aqueous LiFePO4 Cathode Dispersions and Polyethyleneimine Dispersant," *J. Electrochem. Soc.,* vol. 160, pp. A201-A206, 2013.

[97] Y. Yin, "An Experimental Study on PEO Polymer Electrolyte Based All-Solid-State Supercapacitor," Ph. D Thesis Dissertion, University of Miami, Coral Gables, Florida, 2010, Thesis Dissertation.

[98] A. M. Stephan, "Review on gel polymer electrolytes for lithium batteries," *Eur. Polym. J.,* vol. 42, p. 21–42, 2006.

[99] J.-K. Lee, Y.-J. Lee, W.-S. Chae ·Yun-Mo Sung, "Enhanced ionic conductivity in PEO-LiClO4 hybrid electrolytes by structural modification," *J. Electroceram.,* vol. 17, p. 941–944, 2006.

[100] C.W. Lin, C.L. Hung, M. Venkateswarlu, and B.J. Hwang, "Influence of TiO2 nano-particles on the transport properties of composite polymer electrolyte for lithium-ion batteries," *J. Power Sources,* vol. 146, p. 397–401, 2005.

[101] F. Croce, G. B. Appetecchi, L. Persi, and B. Scrosati, "Nano-composite polymer electrolytes for lithiumbatteries," *Nature,* vol. 394, pp. 456-458, 1998.

[102] Y. Wang, J. Travas-Sejdic and R. Steiner, "Polymer gel electrolyte supported with microporous polyolefin membranes for lithium ion polymer battery," *Solid State Ion.,* vol. 148, pp. 443-449, 200.

[103] D.-F. Liu, J. Nie, W.-C. Guan, H.-Q. Duan, and L.-M. Zhuo, "Characterizations of a branched ester-type lithium imide in poly(ethylene oxide)-based polymer electrolytes," *Solid State Ion.,* vol. 167, p. 131–136, 2004.

[104] R. C. Agrawal and G. P. Pandey, "Solid polymer electrolytes: materials designing and all-solid-state battery applications: an overview," *J. Phys. D: Appl. Phys.,* vol. 41, p. 223001, 2008.

[105] B. Scrosati, F. Croce, and L. Persi, "Impedance Spectroscopy Study of PEO-Based Nano-composite Polymer Electrolytes," *J. Electrochem. Soc.,* vol. 147, pp. 1718-1721, 2000.

[106] X. Li, Y. Zhao, L. Cheng, M. Yan, X. Zheng, Z. Gao, Z. Jiang, "Enhanced ionic conductivity of poly(ethylene oxide) (PEO) electrolyte by adding mesoporous molecular sieve LiAISBA," *J. Solid State Electrochem.,* vol. 9, p. 609–615, 2005.

[107] T. M. Ali, N. Padmanathan, and S. Selladurai, "Structural, conductivity, and dielectric characterization of PEO–PEG blend composite polymer electrolyte dispersed with TiO2 nanoparticles," *Ionics ,* vol. 19, p. 1115–1123, 2013.

[108] Y.-H. Li , X.-L. Wu, J.-H. Kim, S. Xin, J. Su, Y. Yan, J.-S. Lee, and Y.-G. Guo, "A novel polymer electrolyte with improved high-tempera turetolerance up to 170 C for high-temperature lithium-ion batteries," *J. Power Sources,* vol. 244, pp. 234-239, 2013.

[109] "Accurate Estimation of Injectability (Syringeability) from High Shear Viscosiy Measurement," Rheosense, San Ramon, CA.

[110] C.-C. Yang, H.-C. Hu, S. J. Lin, and W.-C. Chien, "Electrochemical performance of V-doped spinel Li4Ti5O12/C composite anode in Li-half and Li4Ti5O12/LiFePO4-full cell," *J. Power Sources,* vol. 256, pp. 424-433, 2014.

[111] A. Moretti, G.-T. Kim, D. Bresser, K. Renger, E. Paillard, R. Marassi, M. Winter, and S. Passerini, "Investigation of different binding agents for nanocrystalline anatase TiO2 anodes and its application in a novel, green lithium-ion battery," *J. Power Sources,* vol. 221, pp. 419-426, 2013.